Theses and Dissertations 1. Thesis and Dissertation Collection, all items

2009-09

Investigation of performance improvements including application of inlet guide vanes to a cross-flow fan

Cordero, Samuel F.

Monterey, California. Naval Postgraduate School

http://hdl.handle.net/10945/4531

NAVAL POSTGRADUATE SCHOOL

MONTEREY, CALIFORNIA

THESIS

INVESTIGATION OF PERFORMANCE IMPROVEMENTS INCLUDING APPLICATION OF INLET GUIDE VANES TO A CROSS-FLOW FAN

by

Samuel F. Cordero

September 2009

Thesis Co-Advisors: Garth V. Hobson
                                      Anthony J. Gannon

Approved for public release; distribution is unlimited

THIS PAGE INTENTIONALLY LEFT BLANK

REPORT DOCUMENTATION PAGE		*Form Approved OMB No. 0704-0188*

1. AGENCY USE ONLY *(Leave blank)*	**2. REPORT DATE** September 2009	**3. REPORT TYPE AND DATES COVERED** Master's Thesis
4. TITLE AND SUBTITLE Investigation of Performance Improvements Including Application of Inlet Guide Vanes to a Cross-flow Fan		**5. FUNDING NUMBERS**
6. AUTHOR(S) Samuel F. Cordero		
7. PERFORMING ORGANIZATION NAME(S) AND ADDRESS(ES) Naval Postgraduate School Monterey, CA 93943-5000		**8. PERFORMING ORGANIZATION REPORT NUMBER**
9. SPONSORING /MONITORING AGENCY NAME(S) AND ADDRESS(ES) N/A		**10. SPONSORING/MONITORING AGENCY REPORT NUMBER**

11. SUPPLEMENTARY NOTES The views expressed in this thesis are those of the author and do not reflect the official policy or position of the Department of Defense or the U.S. Government.

12a. DISTRIBUTION / AVAILABILITY STATEMENT Approved for public release; distribution is unlimited	**12b. DISTRIBUTION CODE**

13. ABSTRACT (maximum 200 words)

The inherent characteristics of a cross-flow fan allowing for easy thrust vectoring as well as potential airfoil boundary layer control make it an attractive propulsive means for a theoretical vertical takeoff and landing aircraft. However, to compete with current methods of aircraft propulsion, further performance improvements of the cross-flow fan are needed.

A baseline model of a cross-flow fan geometry developed by Vought Systems in the 1970s was scaled from a 12-inch diameter rotor to a 6-inch diameter rotor as a more realistic size for integration into a fan-in-wing concept to provide both thrust vectoring and boundary layer control over the wing. Using the computational fluid dynamics software ANSYS CFX, baseline performance trends were verified against previous 12- and 6-inch diameter models. Data from this model was then used to design a configuration of inlet guide vanes in an effort to increase the loading on the first stage of the fan and gain an improvement in pressure ratio over the baseline cross-flow fan.

The CFD results were then compared with experimental results from a cross-flow fan test assembly modified to replicate the CFD model with inlet guide vanes. While the application of the particular inlet guide vane configuration did not result in the desired performance improvements, it did validate that computational fluid dynamics can adequately predict the impact of various design changes on the performance of the cross-flow fan as well as provide valuable insight into the behavior of the cross-flow fan for future efforts in performance improvement.

14. SUBJECT TERMS Fan, Cross-flow, Crossflow, Inlet Guide Vanes, Thrust Vectoring, Vertical Take Off	**15. NUMBER OF PAGES** 117
	16. PRICE CODE

17. SECURITY CLASSIFICATION OF REPORT Unclassified	**18. SECURITY CLASSIFICATION OF THIS PAGE** Unclassified	**19. SECURITY CLASSIFICATION OF ABSTRACT** Unclassified	**20. LIMITATION OF ABSTRACT** UU

THIS PAGE INTENTIONALLY LEFT BLANK

INVESTIGATION OF PERFORMANCE IMPROVEMENTS INCLUDING APPLICATION OF INLET GUIDE VANES TO A CROSS-FLOW FAN

Samuel F. Cordero
Lieutenant Commander, United States Navy
B.S.M.E., University of Detroit Mercy, 1997

Submitted in partial fulfillment of the
requirements for the degree of

MASTER OF SCIENCE IN MECHANICAL ENGINEERING

from the

**NAVAL POSTGRADUATE SCHOOL
September 20009**

Author: Samuel F. Cordero

Approved by: Garth V. Hobson
                 Thesis Co-Advisor

                 Anthony Gannon
                 Thesis Co-Advisor

                 Knox T. Millsaps
                 Chairman, Department of Mechanical and Astronautical
                 Engineering

THIS PAGE INTENTIONALLY LEFT BLANK

ABSTRACT

The inherent characteristics of a cross-flow fan allowing for easy thrust vectoring, as well as potential airfoil boundary layer control, make it an attractive propulsive means for a theoretical vertical takeoff and landing aircraft. However, to compete with current methods of aircraft propulsion, further performance improvements of the cross-flow fan are needed.

A baseline model of a cross-flow fan geometry developed by Vought Systems in the 1970s was scaled from a 12-inch diameter rotor to a 6-inch diameter rotor as a more realistic size for integration into a fan-in-wing concept to provide both thrust vectoring and boundary layer control over the wing. Using the computational fluid dynamics software ANSYS CFX, baseline performance trends were verified against previous 12- and 6-inch diameter models. Data from this model was then used to design a configuration of inlet guide vanes in an effort to increase the loading on the first stage of the fan and gain an improvement in pressure ratio over the baseline cross-flow fan.

The CFD results were then compared with experimental results from a cross-flow fan test assembly modified to replicate the CFD model with inlet guide vanes. While the application of the particular inlet guide vane configuration did not result in the desired performance improvements, it did validate that computational fluid dynamics can adequately predict the impact of various design changes on the performance of the cross-flow fan, as well as provide valuable insight into the behavior of the cross-flow fan for future efforts in performance improvement.

THIS PAGE INTENTIONALLY LEFT BLANK

TABLE OF CONTENTS

LIST OF FIGURES

LIST OF TABLES

THIS PAGE INTENTIONALLY LEFT BLANK

LIST OF ACRONYMS AND ABBREVIATIONS

A	Area
ANSYS CFX-Post	Part of the ANSYS CFX Package that Allows for Post Processing of Results Obtained by ANSYS CFX-Solver.
ANSYS CFX-PRE	Part of the ANSYS CFX Package for Application of Boundary and Initial Conditions as Well as Solver Settings.
ANSYS CFX-Solver	Part of the ANSYS CFX Package that Performs the Actual Computations and Allows for Real Time Monitoring of the Solution Status
ANSYS WORKBENCH	Simulation Package Used to Import SOLIDWORKS Files, Create CFX Geometries, Meshing, and Problem Setup for Use by CFX-PRE.
c	Absolute Velocity; equal to blade velocity plus relative velocity of incoming fluid
CFD	Computational Fluid Dynamics
CFF	Cross-Flow Fan
CFL	Courant-Friedrichs-Lewey Number – Used to Indicated Stability in Solving Hyperbolic Partial Differential Equations Using and Explicit Solver; Also Referred to as Courant Number.
CFTA	Cross-Flow Fan Test Assembly
c_p	Specific heat of air at constant pressure
c_θ	Tangential component of absolute velocity; further subscripts denote particular location (blade entrance, blade exit).
DSA	Digital Sensing Array
δ	Non -dimensional total pressure correction term
$\hat{e}$	Internal Energy
F_{Thrust}	Thrust

g	Acceleration due to gravity, 9.81 m/s
GUI	Graphical User Interface
γ	Ratio of specific heats at constant pressure and constant temperature
HPC	High Pressure Cavity – Referred to as "Secondary Vortex Cavity" in Ref [11]
IGV	Inlet Guide Vane
LPC	Low Pressure Cavity – Referred to as "Primary Vortex Cavity in Ref [12]
M	Mach Number
$\dot{m}$	Mass flow rate
NPS	Naval Postgraduate School
N	Shaft speed
η	Efficiency
u	Velocity in the u or x direction, subscript denotes particular location
p	Pressure
P_t	Total Pressure
$\bar{P_t}$	Mass averaged total pressure
π	Non-dimensional ratio of mass averaged total pressure at outlet to total pressure at inlet
ρ	Density
SOLIDWORKS	3-Dimensional Drafting and Solid Modeling Software Package
STOL	Short Take Off and Landing
T	Temperature
T_t	Total Temperature; further subscripts denote particular location
$\bar{T_t}$	Mass averaged total temperature

TPL	Turbo Propulsion Laboratory
TTR	Turbine Test Rig
τ	Non-dimensional ratio of mass averaged total temperature at outlet to total temperature at inlet
θ	Non -dimensional total temperature correction term
U	Blade velocity equal to angular velocity times the radial distance
UAV	Unmanned Aerial Vehicle
V	Velocity
v	Velocity
VSD	Vought Systems Division
VTOL	Vertical Take Off and Landing
W	Relative velocity of incoming fluid flow; subscripts denote particular location (blade entrance, blade exit).
$\dot{W}$	Time rate of change in work, or Power.
X_i	Non Dimensional Velocity at location i
12D	12 Inch Diameter
12D1.5L	12 Inch Diameter, 1.5 Inch Span
6D	Six Inch Diameter
6D1.5L	Six Inch Diameter, 1.5 Inch Span

THIS PAGE INTENTIONALLY LEFT BLANK

ACKNOWLEDGMENTS

THIS PAGE INTENTIONALLY LEFT BLANK

I.   INTRODUCTION

A.   BACKGROUND

The Cross-Flow Fan (CFF) is certainly not a new concept. First patented by Mortier in 1893 [1], the CFF has been used extensively in heating and cooling applications. Additionally, the conceptual application of a CFF to either a short takeoff and landing (STOL) or vertical takeoff and landing (VTOL) type of aircraft is not a new concept either.

In the mid to late 1970s, the Vought Systems Division (VSD) of LTV Aerospace Corporation was contracted by the U.S. Navy to explore new concepts for development of a low subsonic transport aircraft [2]. In execution of this contract, VSD developed 46 different design configurations of cross-flow fans 12 inches (30.48 cm) in diameter with either a 1.5 inch (3.81 cm) or 12-inch (30.48 cm) spans. At the conclusion of testing under the VSD contract, assembly number 6, a 12-inch (30.48 cm) diameter fan with an inlet angle of 105° and an exit duct height of 4.6 inches (11.68 cm), as shown in Figure 1, was determined to be among the more optimal configurations among the 46 different designs.
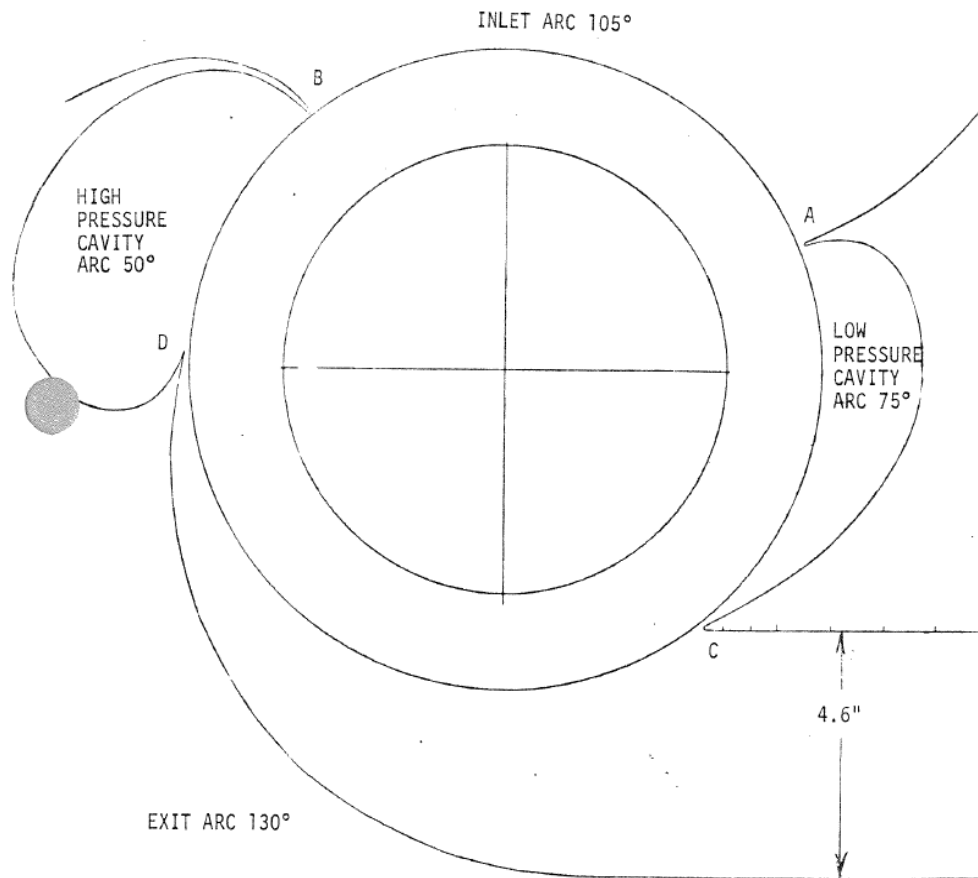
Figure 1.   VSD Multi-Bypass Ratio Propulsion System Fan Housing #6 [From 2]

Upon completion of the VSD contract, little work was done to further investigate the cross-flow fan for propulsive purposes. However, CFF designs for use in the heating, ventilation and air conditioning industries were continuously created and refined. Aside from research conducted in the application of the CFF as a boundary layer control device, little further research was conducted with the CFF as a propulsive device until around the year 2000. Around this time, the Naval Postgraduate School, Syracuse University, and Fan Wing LTD began new efforts towards the application of the CFF as a propulsive means for STOL and VTOL aircraft.

Research at the Naval Postgraduate School (NPS) by Seaton [3] Cheng [4], Schreiber [5], Yu [6], and Ulvin [7] as well as Gannon, Utschig, Hobson, and Platzer [8] involved investigations of the performance characteristics and suitability for VTOL

propulsion via cross-flow fans in either 6-inch (15.24 cm) or 12-inch (30.28 cm) diameter fans with 30 double circular arc blades modeled after the VSD configuration #6 maintaining a 0.70 inner to outer diameter ratio.

Elsewhere, researchers and entrepreneurs at FanWing LTD have incorporated a cross-flow fan into the leading edge of a propulsive wing for an unmanned aerial vehicle (UAV) [9]. Additionally, Kummer and other researchers at Syracuse University have been continuously investigating the application of a CFF in the trailing edge of a modified Gottingen 570 airfoil for lift enhancement, flow control and thrust production [10, 11].

B.   CURRENT STUDY

Starting with the proposal by Gossett [12] to incorporate a CFF as an augmentation device for vertical thrust in a single seat VTOL aircraft, researchers at both the Naval Postgraduate School and Syracuse University have urged further investigations into various configurations of the CFF in an effort to improve performance.

Research at the Naval Postgraduate School initially started with verification of the VSD data, as well as initial Computational Fluid Dynamics modeling by both Seaton [3] and Cheng [4]. Both Seaton and Cheng tested and modeled 12 inch (30.28 cm), 1.5-inch (3.81 cm) span CFFs modeled after the VSD configuration #6 as shown earlier in Figure 1. Seaton's data verified the data obtained by VSD. However, while VSD data was from 6000 rpm and higher, Seaton's data included runs from 2,000 rpm and above. From this, Seaton concluded that at 3250 rpm, a thrust to power ratio of 2 vice 1.5 at 6,500 rpm measured by VSD could be obtained. Seaton also proposed the incorporation of the CFF into a wing as means to generate more total thrust due to the increased specific thrust output of the CFF at these lower rotational speeds [3].

While Seaton was only able to model a 15-blade rotor [3], Cheng set out to model and verify experimentally an accurate 30-blade model. Cheng also set out to experimentally investigate the effects of blocking off different combinations of the low and high-pressure cavities as displayed in Figure 1, as well as to investigate the behavior of the CFF under exhaust flow throttling. Cheng largely found that overall efficiency

was highest in the case with the high-pressure cavity (HPC) left open and the low-pressure cavity (LPC) closed. The lowest observed efficiency as well as the highest observed total temperature ratio was with both cavities open. Total pressure ratios were nearly identical for all permutations of the cavities closed or open except for the case of both cavities being closed. With both cavities closed, a decrease (albeit slight) in total pressure ratio was observed. Ultimately, Cheng was able to demonstrate that CFD could accurately depict the flow patterns of the cross-flow fan [4].

Gannon, Utschig, Hobson, and Platzer then investigated diametrical scaling laws for the CFF. Tests were conducted using the same 12-inch (30.28 cm) diameter fan used by Seaton and Cheng, as well as a similar version scaled to 6 inches (15.14 cm) in diameter. In addition to validating modified scaling laws, they obtained compressor maps for the fans by measuring performance parameters at various discharge throttling rates (thus varying mass flow rates) [8].

Continuing research by Schreiber at the Naval Postgraduate School built upon the scaling research by Gannon et al. and investigated span wise scaling laws. Schreiber set out to investigate scaling laws for the 6 inch (15.24 cm) diameter, 1.5 inch (3.81cm) span (6D1.5L) CFF and the 6 inch (15.24cm) diameter, 6 inch (15.24cm) span (6D6L) CFF. Although failure of the 6D6L fan occurred when operating above 4,700 RPM, Schreiber was able to make comparisons between the 6D1.5L and 6D6L CFFs at 2,000, 3,000, 4,000, and 4,500 RPM. Schreiber was able to conclude the following [5]:

- 1:1 ratio between both fans in terms of specific thrust per until length

- 0.86 ratio (6D1.5L to 6D6L) of mass flow rate per unit span

- 0.96 ratio (6D1.5L to 6D6L) of thrust to power per mass flow rate per unit span

- Generally 3-9% higher efficiencies for the 6D6L CFF vs. the 6D1.5L CFF

Yu then principally continued the CFD modeling effort of the CFF at the Naval Postgraduate School. Earlier CFD models had used incompressible solvers, and Yu set out to more accurately model the flow with ANSYS CFX, which is capable of modeling

compressible flow. Additionally, with new sensor arrays, Yu obtained new experimental data was from the 12-inch (30.48cm) diameter 1.5 inch (3.81cm) span fan (12D1.5L) and compared against the CFD results with favorable agreement between experiment and CFD simulation [6].

At Syracuse University, CFF research has been carried out principally by Dang and Kummer. However, Kummer's Ph.D. Dissertation is perhaps the most extensive collection of investigation into the performance of the CFF from Syracuse University to date. Computationally, Kummer conducted parametric studies on various housing configurations as well as a comparison between the VSD double circular arc blade design and a constant thickness squared end blade. Kummer's findings via CFD agree with experimental results of Cheng such that higher efficiencies were obtained when closing off the LPC and leaving the HPC open however with a slightly larger increase (10% for Kummer and 8% for Cheng). Kummer also documented a noticeable (6%) decrease in efficiency when increasing the tip gap from 1.5% to 10%. In terms of blade shape, Kummer found that squared blade ends had the largest effect on performance while double circular arc vs. constant thickness had a smaller (but quantifiable) effect on performance [10].

In all of the above listed research, one theme continues: continue investigation into fan and housing designs in an effort to find a more optimally performing fan that can be competitive with existing aircraft propulsion technologies.

C.   RESEARCH AIMS

In order to continue development of the CFF for use in a VTOL aircraft, a key performance parameter of the CFF in need of improvement is that of thrust. If one were to use Equation (1) to determine thrust while assuming the aircraft is at rest attempting to take off vertically such that $u_{in} = 0$ and mass flow rate is constant, one can see that thrust is directly proportional to exit velocity, u_{out}.

$$F_{Thrust} = \dot{m}\left(u_{out} - u_{in}\right) \qquad (1)$$

5

The question then arises as to how we can maximize exit velocity. If one were to apply a simplified control volume approach to a CFF embedded in a wing like that shown in Figure 2 and initially treat the flow as incompressible for simplicity, then using the following equations from [13], it can be shown that thrust is a function of pressure ratio across the CFF:

$$\dot{W}_{Shaft,1-2} = \dot{m}\left[\left(\hat{e}_2 - \hat{e}_1\right) + \left(\frac{p_2}{\rho} - \frac{p_1}{\rho}\right) + \frac{V_2^2 - V_1^2}{2} + g\Delta z\right] \tag{2}$$

Since internal energy ($\hat{e}$) and pressure at points 1 and 2 in Figure 2 are equal, Equation (2) simplifies to :

$$\dot{W}_{Shaft,1-2} = \dot{m}\left(\frac{V_2^2}{2}\right) \tag{2b}$$

Because the work on the system in either control volume must be equal, the application of Equation (2) to the control volume around the CFF yields:

$$\dot{W}_{Shaft,3-4} = \dot{m}\left[\left(\hat{e}_4 - \hat{e}_3\right) + \left(\frac{p_4}{\rho} - \frac{p_3}{\rho}\right) + \frac{V_4^2 - V_3^2}{2} + g\Delta z\right] \tag{3}$$

Where Equation (3) can be simplified to:

$$\dot{W}_{Shaft,3-4} = \dot{m}\left(\frac{p_4 - p_3}{\rho}\right) \tag{3b}$$

Equating the simplified version of Equations (2) and (3) and simplifying yields:

$$\dot{W}_{Shaft,1-2} = \left(\frac{V_2^2}{2}\right) = \dot{W}_{Shaft,3-4} = \left(\frac{p_4 - p_3}{\rho}\right) \tag{4}$$

If we take $V_2 = u_{out}$ from Equation (1), we can clearly see that F_{Thrust} is directly proportional to the pressure ratio from point 3 to point 4 in Figure 2.
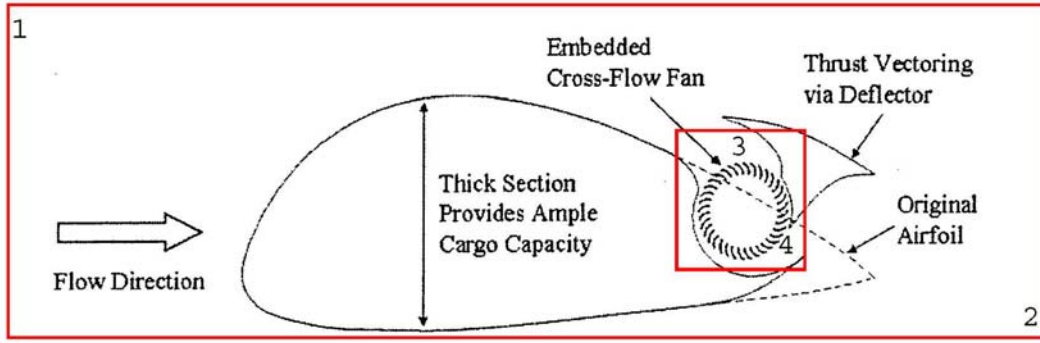
Figure 2.   Control Volumes for Analysis of Thrust from a CFF embedded in a wing
[After 10]

Further, the work performed can be equated to the following, also from [13]:

$$\dot{W}_{Shaft} = -\dot{m}_{in}\left(\pm U_{in}V_{\theta in}\right) + \dot{m}_{out}\left(\pm U_{out}V_{\theta out}\right) \tag{5}$$

Modifying Equation (4) to agree with the geometry and terminology of Figure 3 as well as assuming mass flow rate is constant throughout yields the following:

$$\dot{W}_{Shaft} = \dot{m}\left(U_4 c_{\theta 4} - U_1 c_{\theta 1}\right) \tag{5a}$$

Setting Equation (5a) equal to Equation (3b) yields the following relation between pressure ratio, angular velocity (U), and tangential velocity (c_θ):

$$\left(U_4 c_{\theta 4} - U_1 c_{\theta 1}\right) = \left(\frac{p_4 - p_3}{\rho}\right) = \frac{\Delta p}{\rho} \tag{6}$$

Figure 3 shows velocity triangles for what is considered both the first stage (fan inlet) and second stage (near the fan outlet). If only attempting to increase blade loading on the first stage and using subscripts (1) and (2) to denote the first stage blade leading and trailing edges respectively, Equation 6 can be re-written in terms of the first stage blades only:

$$\left(U_2 c_{\theta 2} - U_1 c_{\theta 1}\right) = \left(\frac{p_2 - p_1}{\rho}\right) = \frac{\Delta p_{FirstStage}}{\rho} \tag{6b}$$

7
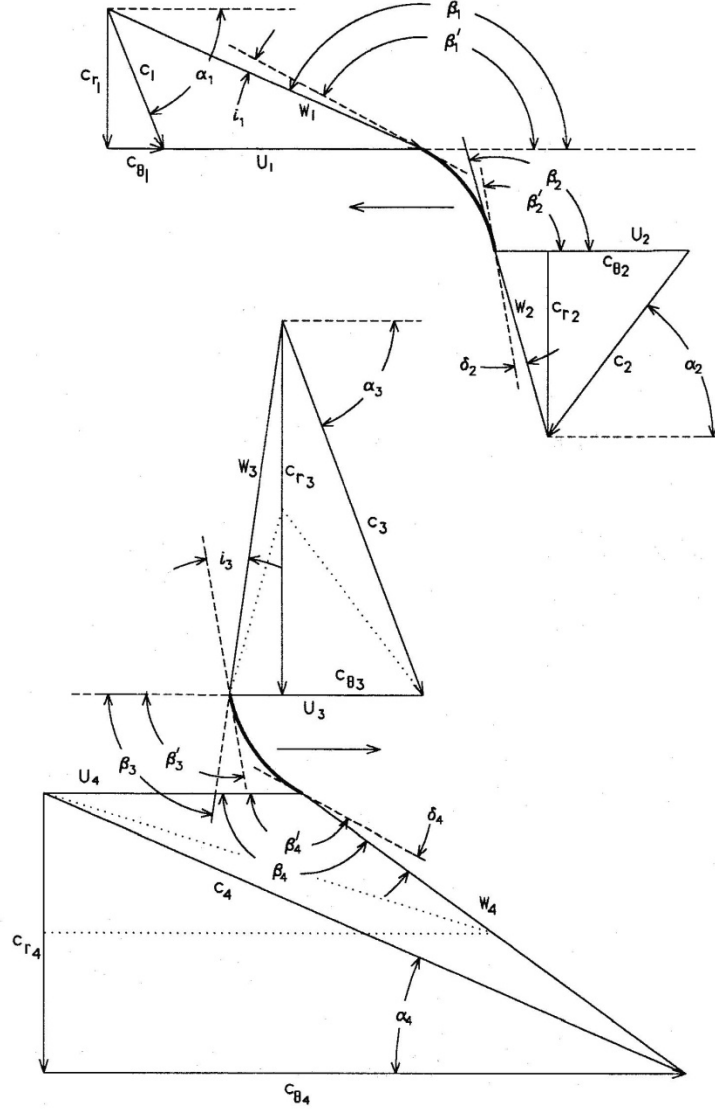
Figure 3.   Velocity Triangles for 1st and 2nd stage blades [From 10]

Analyzing Figure 3 in conjunction with Equation (6), it can be shown that increasing the pressure ratio can be achieved by increasing the difference between $c_{\theta 2}$ and $c_{\theta 1}$. Without changing blade geometry or configuration, the most obvious method to increase the difference between $c_{\theta 2}$ and $c_{\theta 1}$ is to alter the flow into the 1st stage of the CFF such that the $c_{\theta 1}$ component is larger. That is to say, control the incoming flow such that the flow more closely impinges on or opposes the direction of blade motion. Since

$c_{\theta 1}$ is in the opposite (negative) direction of $c_{\theta 2}$, when Equation (3) is applied, a larger negative value of $c_{\theta 1}$ yields a larger value of pressure increase. Going back to equation (4), a larger pressure ratio yields a larger exit velocity. Assuming mass flow rate remains constant, this larger exit velocity can yield more thrust as shown earlier in Equation (1).

Thus, the aim of this research was to model the baseline CFF configuration that was tested by Gannon et al. in [8] using ANSYS CFX in order to obtain information on CFF flow field characteristics to help select an appropriate inlet guide vane (IGV) configuration such that a larger change of tangential velocity components would yield a larger pressure ratio and subsequent increase in thrust.

THIS PAGE INTENTIONALLY LEFT BLANK

II.   COMPUTATIONAL MODEL

A.   OVERVIEW

The concept of developing a computational fluid dynamics (CFD) model for use in parametric studies of differing design configuration of a cross-flow fan (CFF) is certainly appealing. Earlier effort by Yu used ICEM-CFD for geometry and grid generation and then ANSYS CFX for problem setup and analysis. While Yu's model displayed results that compared favorably with experimental results [6], the method employed for geometry and subsequent structured mesh development appeared to be quite labor intensive and thus not as amenable to quick design changes for parametric studies.

For the reason outlined above, models developed in SOLIDWORKS were developed and exported to ANSYS WORKBENCH for unstructured grid generation. The CFD software package ANSYS CFX 5 was then used for problem definition, solution and post processing in a fashion as similar as possible to that of Yu in [6].

B.   GEOMETRY AND GRID GENERATION

Individual solid models for both the 6 inch (15.24cm) diameter 1.5 inch (3.81cm) span (6D1.5L) fan and the housing similar to the fan tested by Gannon et al. in [8] was created using SOLIDWORKS. Additionally, volumes equal to the outer dimensions of both the fan and the housing were created in SOLDIDWORKS. Utilizing the ANSYS WORKBENCH export feature of SOLIDWORKS, the various solids (fluid volumes) were exported to ANSYS workbench for generation of the fluid domain geometries and subsequent meshing.

In the DESIGN MODELER portion of ANSYS WORKBENCH, first the solid disc corresponding to the outer dimensions of the fan was imported. However, in an effort to keep the overall number of elements in the computational grid to a reasonable number, as well as to try to treat the model as 2-D, the width of the solid disc was thinned to a width of $1/16^{th}$ of an inch (1.59mm). Using the ADD/SUBTRACT GEOMETRY feature in ANSYS WORKBENCH, the fan solid model was imported as a SUBTRACT

feature from the solid disk. This created a solid model of the fluid domain surrounding the blades of the fan itself. Similar methodology was used with the fan housing and one geometry file was created with two domains: the FAN DOMAIN (rotating) and CASING DOMAIN (stationary) are shown in Figures 4(a) and 5(b).

(a)   (b)
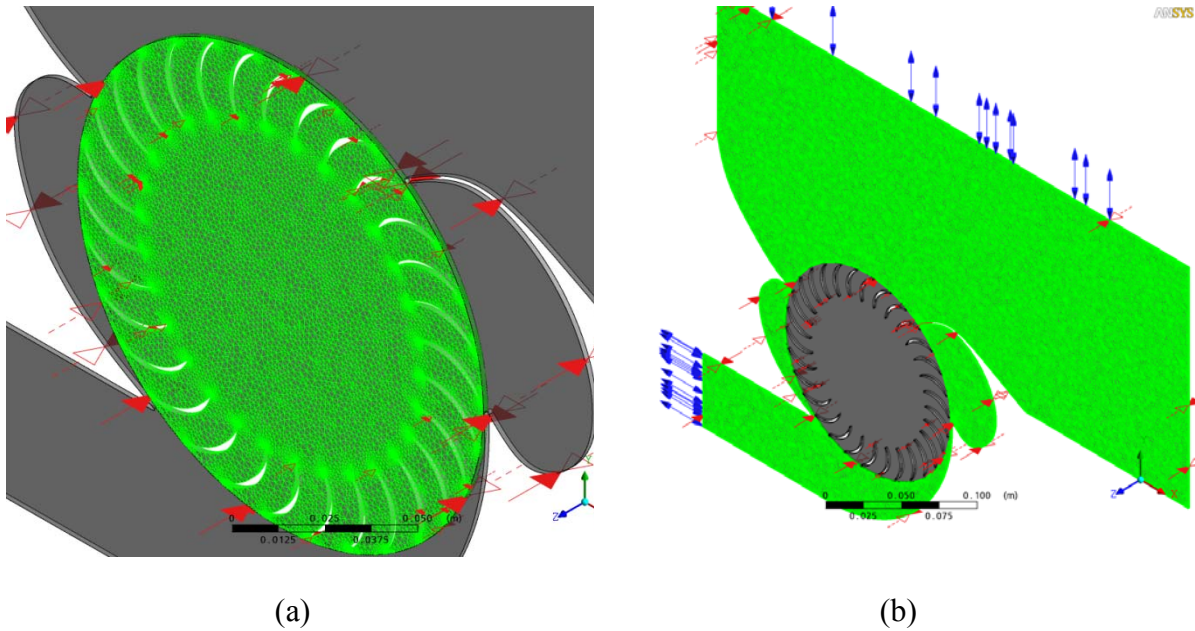
Figure 4.   (a) Baseline Fan Domain mesh and (b) Baseline Casing Domain mesh.

The meshing tool in ANSYS WORKBENCH was used to generate volume meshes for both domains.   Because ANSYS WORKBENCH meshing uses an unstructured grid, point controls were used when needed in areas that did not appear to have sufficient mesh refinement.   Typically, these areas were regions with tight clearances. A typical application of point control usage for desired mesh refinement in one of these areas on the base line model is shown in Figure 5.
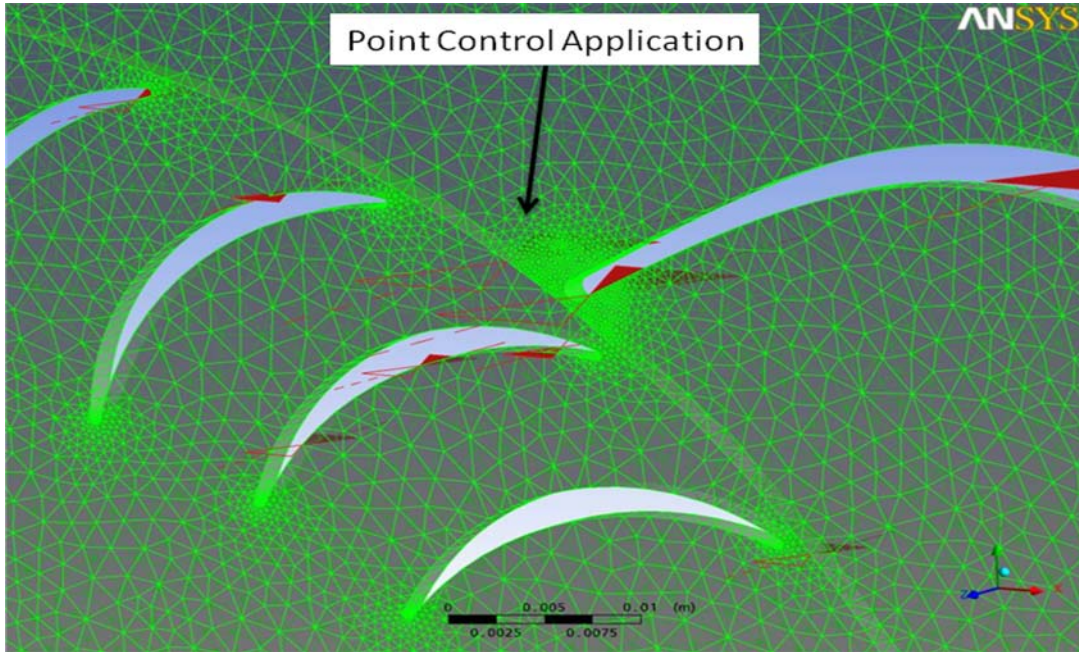
Figure 5.   Illustration of Pont Control Application on the baseline model

The baseline model was built as a 3-D model with a thickness $1/16^{th}$ of an inch (1.59mm) and a maximum number of elements across a gap equal to 2, again in an effort to treat the simulation as a 2-D model as much as possible. Because the number of elements for the baseline model was around 750,000 elements with computational times on the order of one day per revolution, the application of inflation layers to better capture boundary layer behavior was concluded to be excessively computationally expensive. However, when building subsequent models, it was discovered that the application of a 2-D extruded meshing strategy could be used on the CASING DOMAIN. Using this 2-D meshing strategy, the number of overall elements was greatly reduced in the CASING DOMAIN and allowed the implementation of inflation layers on later models while keeping computation times on the order of one day per revolution. Attempts to apply the 2-D extruded meshing strategy to the rotor or fan portion were unsuccessful and thus the 3-D meshing strategy on the fan was retained from the original baseline model. It is believed that the method of creating a solid disc of the fluid domain and cutting the blades out of another solid model while in the DESIGN MODELER function of ANSYS WORKBENCH was the crux of the problem in applying the 2-D mesh to the rotor.

13

A procedure for generating the baseline ANSYS WORKBENCH model and volume mesh is provided in Appendix A.

C.   METHODOLOGY AND BOUNDARY CONDITIONS

With the previous favorable efforts of Yu in using ANSYS CFX to predict performance of the CFF, much of the methodology and boundary conditions from his simulations were repeated for consistency and restated here for completeness [6].

Due to the flow field in the CFF being unsteady, transient solutions were carried out for simulation of the CFF. This was accomplished by defining the interface regions between the rotational and stationary domains as "Transient Rotor-Stator." The transient rotor-stator and related transient initialization allowed for the solver to be started without interpolating initial values. The default values were used instead by selecting transient initialization override.

The working fluid was specified as air-ideal gas with constant specific heat at constant pressure. Reference pressure was set at 1 atmosphere while the opening inlet and outlet boundary conditions were set to an average relative pressure of 0 atmospheres. The inlet and outlet were specified with the opening boundary condition due to uncertainties regarding recirculation at the boundaries, particularly at start up. Static temperature at the inlet and outlet was specified as 300 K, while turbulence intensity factor was set at 5% for both inlet and outlet as well. The adiabatic no slip wall condition was set for all wall surfaces. The symmetry condition was applied to the surfaces lying in the x-y plane with symmetry applied in the positive and negative z-directions with fan rotation about the z-axis.

Equations used by the solver included continuity, momentum, energy, turbulence eddy dissipation, turbulent kinetic energy, and an equation of state. In order to include the effects of turbulence and heat transfer, the k-epsilon turbulence and total energy models were applied.

With much of the preceding nearly identical to the methodology used by Yu [6], The current study did, however, deviate from Yu's methodology in that adaptive time

14

step selection was used in addition to enabling compressibility controls with high speed numerics. Yu's time step for the 2-D model of the 12-inch (30.24 cm) diameter (12D) fan at 3,000 rpm was fixed at 5.5e-5 seconds [6]. Additionally, Kummer suggested that a time step selection of 1/20th of the blade passing period as adequate [10]. Using Kummer's time step selection, that would correspond to 3.3e-5 for a 30 bladed rotor at 3000 rpm.

While Yu and Kummer modeled the 12D CFF, both of them used structured 2-D meshes with Yu's model comprised of 62,493 elements and Kummer's model was 132,000 cells [6, 10]. Models for the current study of the 6D CFF with an unstructured mesh ranged from approximately 750,000 elements to about 850,000 elements with a 2D mesh for the fan casing and a 3-D mesh for the CFF itself. While ANSYS CFX is an implicit solver and, thus, not as dependent on Courant or CFL Number for stability when solving steady state solutions, the transient nature of the CFF solution requires at least an upper bound on the Courant Number. The influence of Courant Number on solution stability was seen in initial attempts to model the CFF using an unstructured mesh in which solutions appeared to begin to diverge using fixed time steps on the order of what Yu used [6].

Given that the size of the elements decreases when the number of elements increase as well as having a physically smaller model with partial 3D modeling, the time step must be smaller in the present study when compared to that of Yu and Kummer [6,10]. For simplicity in selecting an appropriate time step, the option of adaptive time stepping constrained to an upper limit of 1 for the root mean square Courant Number was selected. Initial time step was set at 8e-6 seconds with a lower limit of 1e-7 seconds.

The final deviation from Yu's methodology was the enabling of compressibility controls with high-speed numerics. While Yu's model at twice the diameter has twice the tip speed of the 6D CFF for the same rpm, it was observed that his model yielded Mach numbers around 0.3. With this in mind for future higher speed simulations on the 6D CFF, compressibility controls with high speed numerics was enabled with little penalty to computational time.

D. SIMULATION PLANS

As mentioned earlier, a 3D model of the 6D1.5L CFF was created in solid works. In an attempt to approximate a 2D simulation as much as possible, the thickness of the model was reduced from 1.5 inches (3.81 cm) to 1/16th inch (0.15875 cm). With a much finer mesh in comparison to the larger 12D CFF CFD models of Yu [6] and Kummer [10], the baseline model simulation was conducted at 3000 rpm to verify results and gather data to be used in the development of various design configurations. Due to the fine mesh, speeds higher than 3,000 rpm would have likely resulted in excessively long computational times.

Following the baseline simulation, additional models were created to further investigate impacts on performance. Since it was believed a more realistic model for an aircraft application would have a horizontal inlet vice vertical inlet, the changes from baseline were incrementally developed so as to identify causes for changes in performance to a single design change. All models used the same or as similar as possible mesh settings as the baseline model. All solver and simulation settings remained the same. Table 1 summarizes the various computational models.

Computational Model Designation	Deviation Features from the baseline Model
A	None – baseline model
B	Horizontal Inlet vice Vertical Inlet
C	Cavities Removed with Horizontal vice Vertical Inlet
D	6 Inlet Guide Vanes added with Horizontal Inlet
E	7 Inlet Guide Vanes, Horizontal Inlet, No cavities, 130 degree fan inlet arc vice 105 degree, rounded casing.

Table 1.   Computational Model Designations and Design Configurations

E.   BASELINE CFD MODEL RESULTS

1.   Model Validation

In order to properly compare the CFD model with experimental results, one must attempt to replicate as much as possible the sampling methods used in the experiment. To that aim, using ANSYS CFX POST, probe data was taken in the exhaust duct from the CFD model from locations identical to those in the experiment. Likewise, the same formulation to arrive at CFF performance indicators was used with the data obtained at the probe locations in ANSYS CFX POST. Figure 6 shows the pressure probe location for the experimental setup, while Figure 7 shows the probe location in the exit duct of the computational model. Formulations for determining mass averaged properties of the flow field can be found in Chapter III.
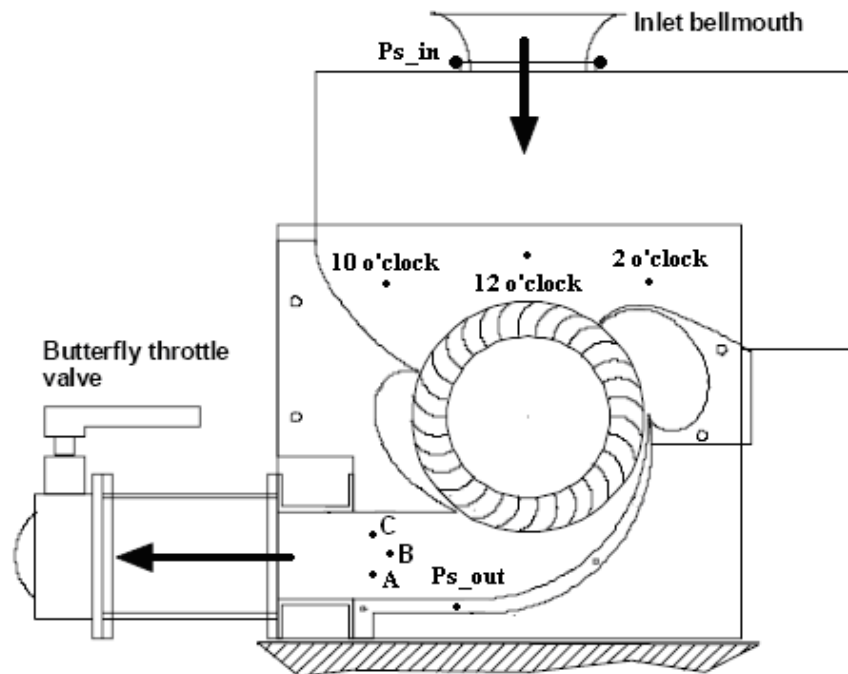
Figure 6.   Location of Combination Probes and Static Pressure Taps for
Experimental Setup [From 7]
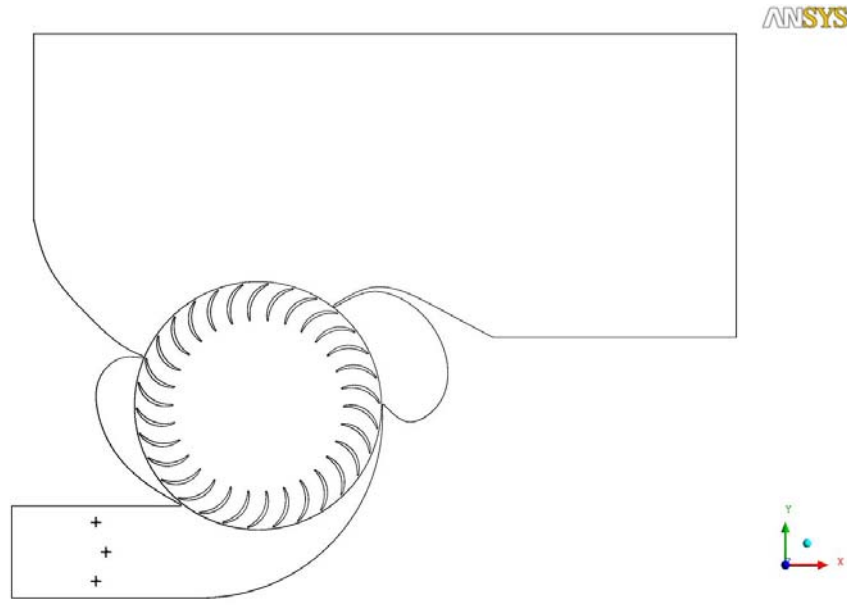
Figure 7.   ANSYS CFX POST Probe Locations

As the solver settings were similar to that of Yu, so too was the behavior of the model. In early revolutions, the flow field was quite unstable as were the flow field properties. Subsequent revolutions lead to a steadying trend in flow field properties, with performance parameters calculated from these properties eventually approaching asymptotic values by the 10th revolution. Figure 8 shows calculated values of efficiency based on mass averaged total temperature and pressure ratios for both the present study, as well as data from Yu [6]. As seen in Figures 9 and 10, total temperature and total pressure ratios were thus quite similarly behaved, but with different ratio values due to the size difference of the fans (6 inch fan in the present study and 12 inch fan in Yu's study).
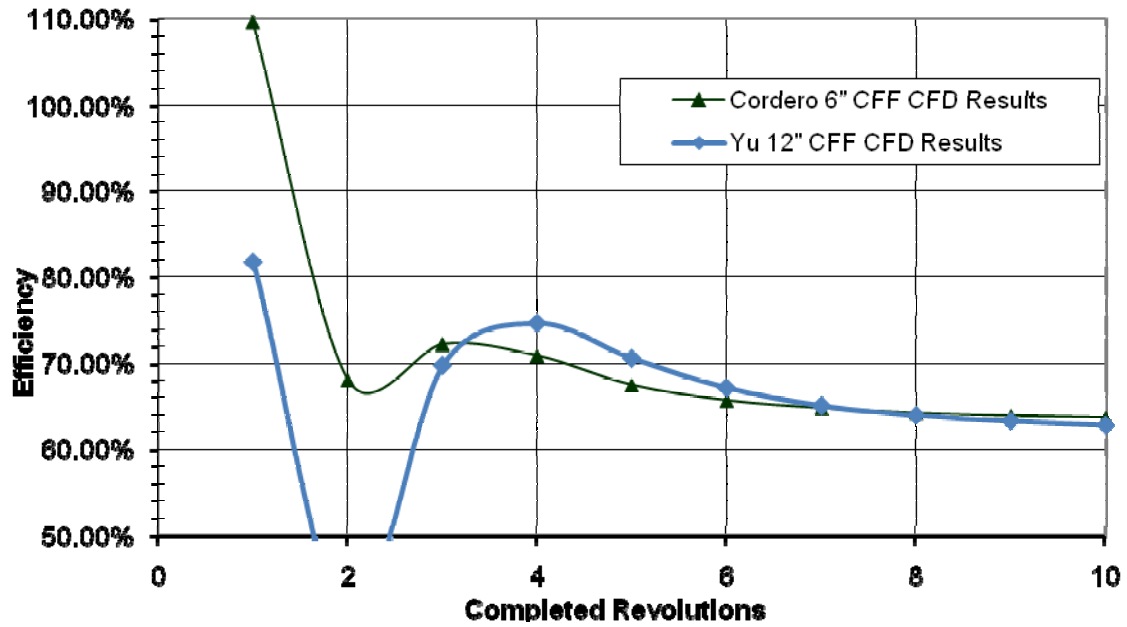
Figure 8.   CFD Efficiencies versus Completed Revolutions for both Cordero and Yu
with data [From 6]
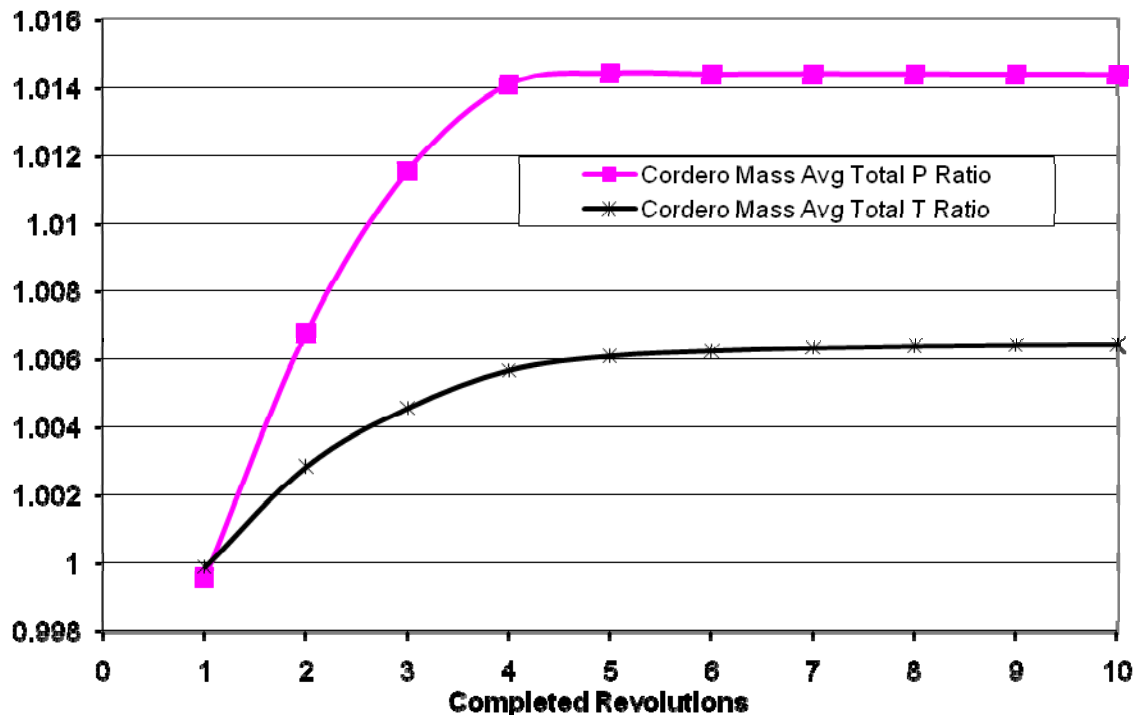
Figure 9.   6" CFD Mass Averaged Total Pressure and Temperature Ratios
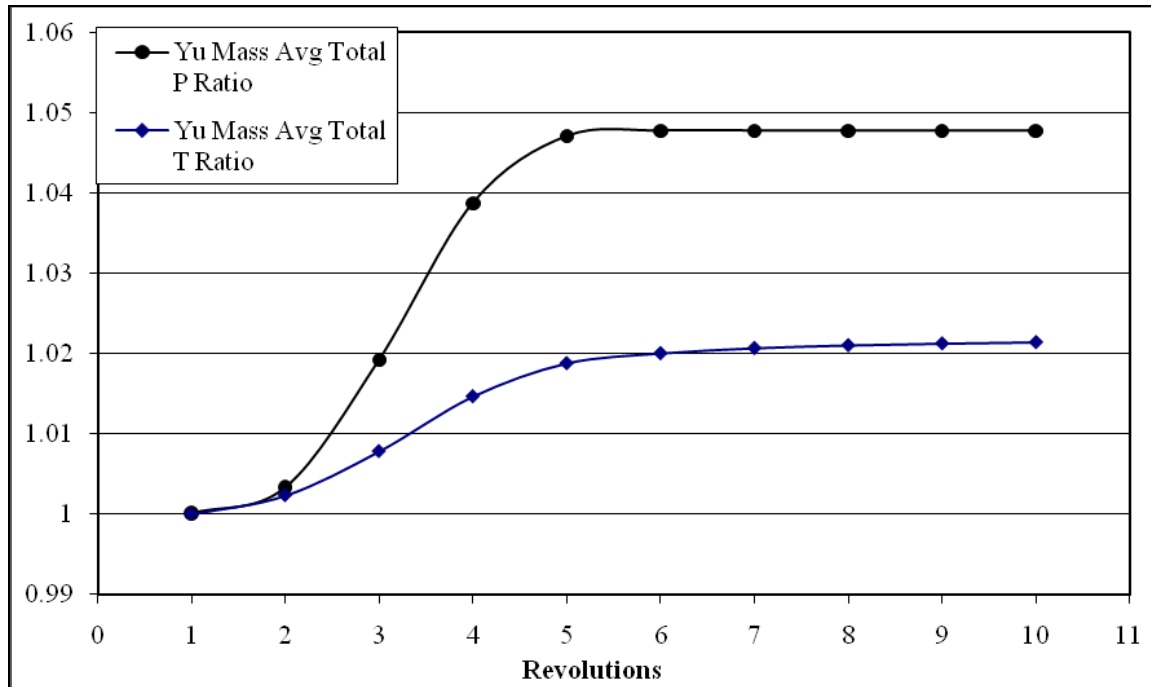
Figure 10.   12" CFD Mass Averaged Total Pressure and Temperature Ratios
[From 6]

Comparison of the model to the most recent experimental results of the 6-inch (15.24 cm) CFF in a 4-inch (10.16 cm) span by Ulvin shows reasonableness of the model as well. With the CFD model yielding a final efficiency of 63.7% in an un-throttled condition corresponding to a mass flow rate normalized to a unit length of span equal to 3.05 kg/(sec·m), this result can be compared to Ulvin's data from [7] shown in Figure 10. Initially, the 63.7% returned from the CFD model does not appear to agree that favorably with the data presented in Figure 7. However, if one applies the findings of Schreiber in which efficiency between the 6D1.5L and 6D6L fans differed by 3 to 9%, one could apply a similar scaling to the 6D4L data shown in Figure 10 [5]. Further, in Figure 11, Schreiber reproduces data from Gannon et al. in [8] for the 6D1.5L CFF in which there is considerably closer agreement at the normalized 3.05 kg/(sec·m) mass flow rate.

20
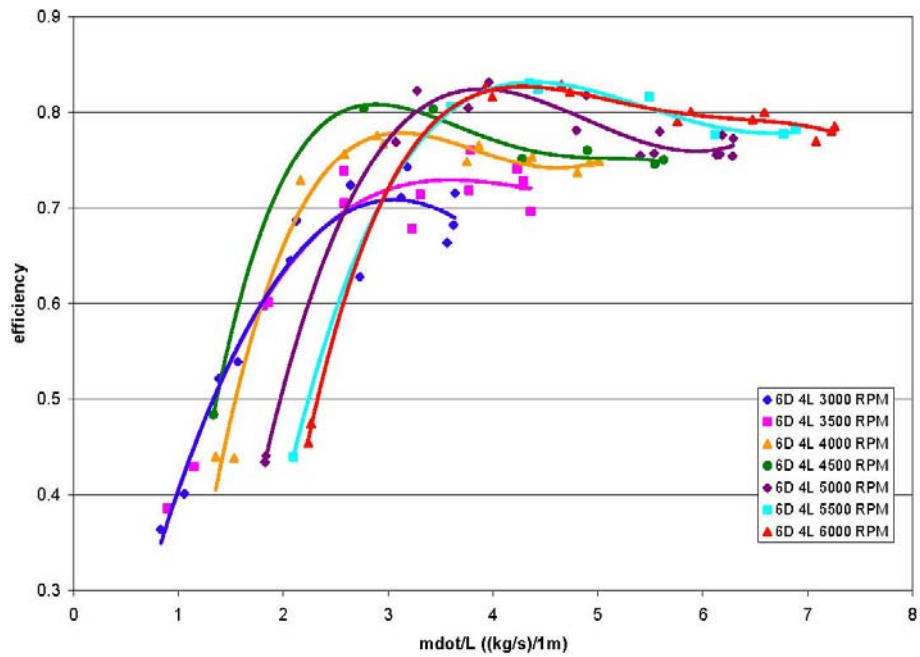
Figure 11.   6D4L Efficiency Map, from [7]
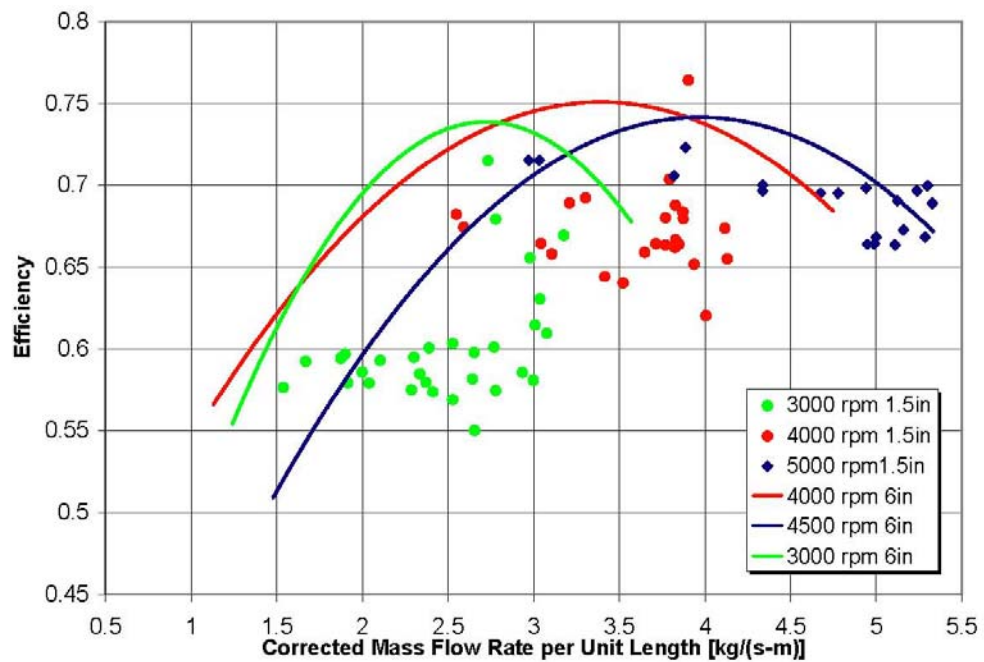
Figure 12.   6D1.5L and 6D6L Efficiency Map [From 5]

21

2. Inlet Guide Vane Design Data

Once the CFD model was verified to represent a reasonable simulation of the actual CFF, data from the CFD model was used to help select a possible IGV design configuration for further modeling. Using the method of acquiring data via probe locations in ANSYS CFX POST, velocity component data was taken in five representative locations across the 105-degree inlet arc of the CFF. Figure 13 shows the locations where the probe data was obtained. Figure 14 shows the decomposed velocity components at those locations while Table 2 lists the u and v direction velocity components at each probe location.
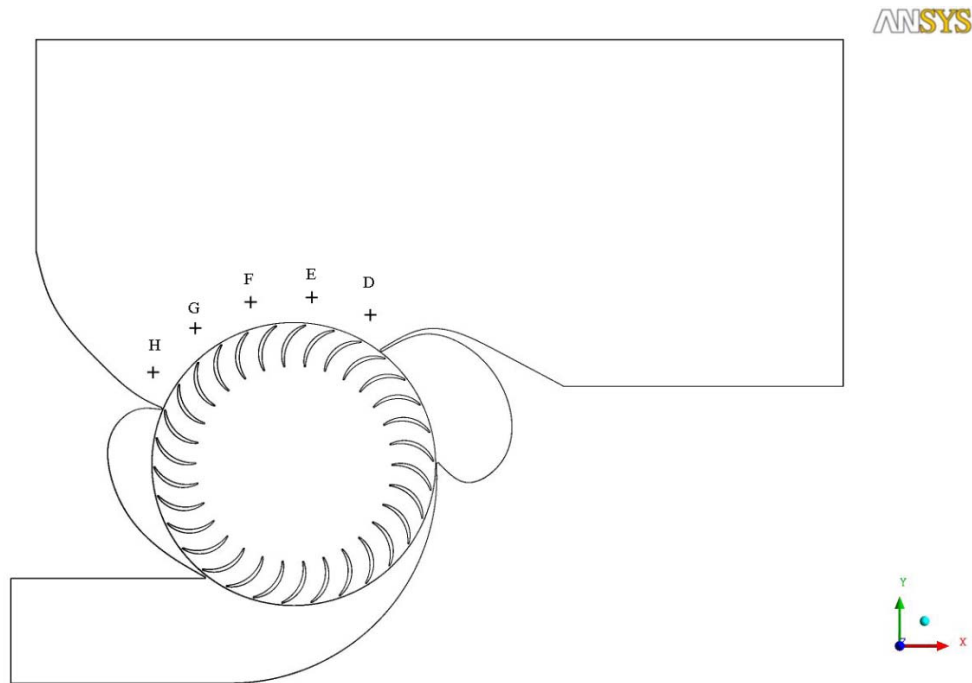
Figure 13. ANSYS CFX POST Inlet Probe Locations
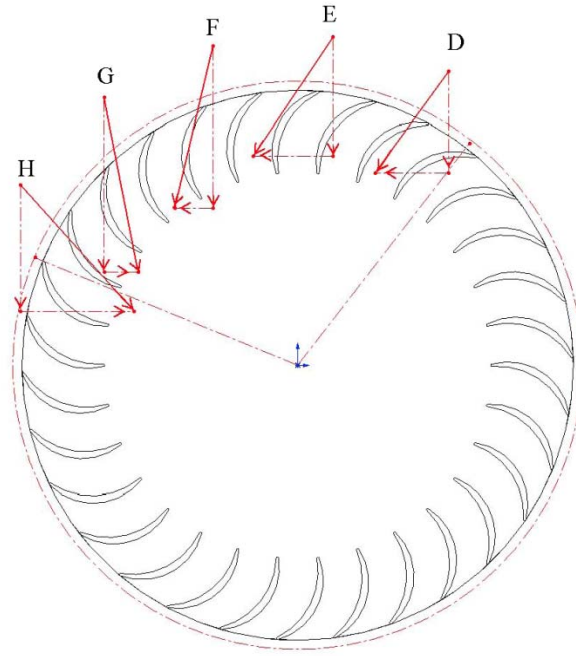
Figure 14.   Baseline Model Velocity Components at Fan Inlet

Probe Location	u-component velocity (m/s)	v-component velocity (m/s)
D	-11.640	-8.817
E	-8.679	-12.930
F	-4.152	-17.62
G	3.728	-19.04
H	12.390	-13.280

Table 2.   Baseline Model Velocity Components at ANSYS CFX POST probe locations.

Further investigation of Figure 14 and Table 2 with the previously made arguments made of Chapter I.C showed that most of the mean line flow on average only 20 degrees from radial. This was further confirmed when viewing the stream lines of the flow, as seen in Figure 15.
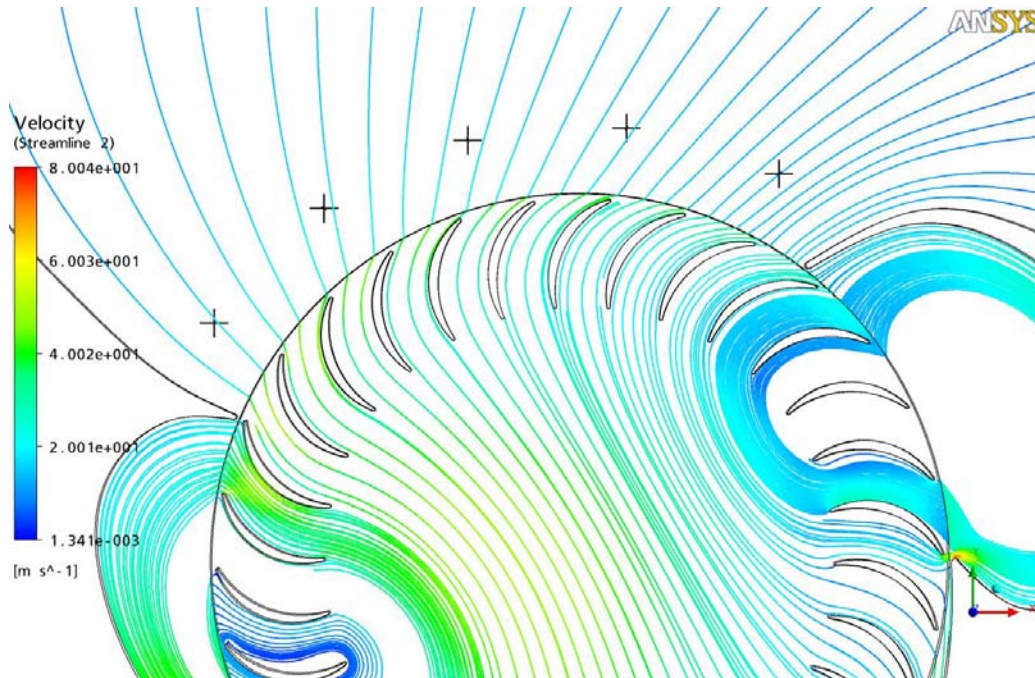
Figure 15.   Close in View of Streamlines for Baseline Model Showing Near Radial Inlet

Using the decomposed velocity vectors of Figure 14, Table 2, and the streamline visualization of Figure 15, a conceptual inlet guide vane configuration was developed. It was decided to remain close to the same chord length scale on the IGVs as the blades in the fan. Similar leading and trailing edge radii were chosen as well. Using the spline feature in SOLIDWORKS, a blade profile was created that was close in dimensions to the double circular arc of the fan blades, but an attempt was made to give it a thicker cross section on the leading edge side of mid chord versus the trailing edge side of mid chord. The inlet guide vanes were then centered the probe locations shown in Figure 15. Using the circular pattern feature in SOLIDWORKS, one individual guide vane was repeated in a circular fashion, ultimately with 6 IGVs spaced 14.4 degrees apart over the 105-degree fan inlet arc. Figure 16 shows an isometric and cross section view of a single IGV with units in inches, while Figure 17 shows the IGVs cut out from the fluid domain within the fan casing/housing.
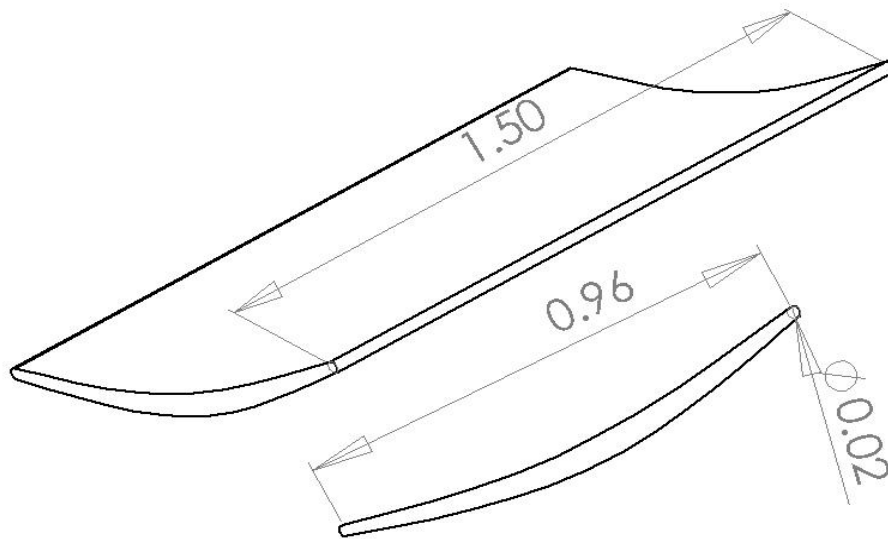
Figure 16.   Inlet Guide Vane Section View
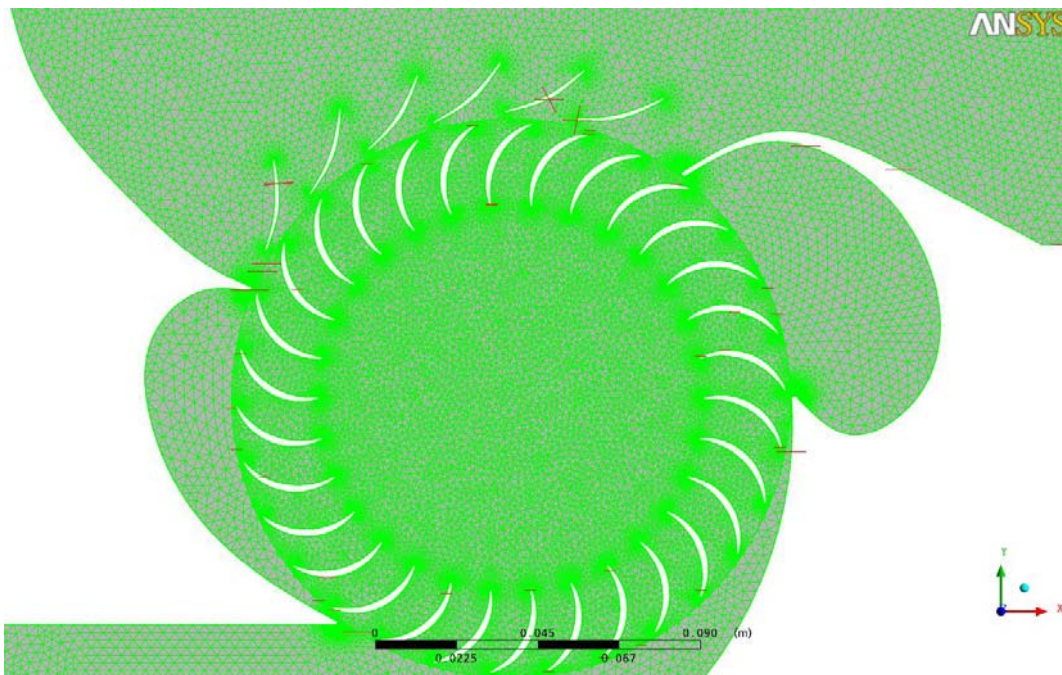
Figure 17.   IGV Cut Out from Fluid Domain

THIS PAGE LEFT INTENTIONALLY LEFT BLANK

III. EXPERIMENTAL SETUP

A. EXPERIMENTAL APPARATUS

1. Cross-Flow Fan Test Assembly (CFTA)

The Cross-Flow Fan Test Assembly (CFTA) used for testing was similar the VSD assembly #6 in that it consisted of 30 double circular arc blades, a 0.70 diameter ratio, a 105 degree inlet arc, and similarly shaped and positioned High Pressure Cavity (HPC) and Low Pressure Cavity (LPC). The particular CFTA used for this experiment was the 6 inch (15.24cm) diameter, 1.5 inch (3.81cm) span (6D1.5L) and was the same fan and housing (inlet, exhaust, HPC and LPC) used by Gannon et al. in [9]. An inlet bell mouth with a 3.25-inch (8.26 cm) diameter throat was used to measure mass flow rate in both vertical and horizontal inlet configurations while a butterfly valve in the exhaust duct was used for throttling studies. Figure 18 shows the horizontal inlet configuration.

Figure 18.   CFTA with Horizontal Inlet

27

For purposes of inlet guide vane (IGV) testing, IGVs of the profile used in the numerical model were machined out of billet aluminum stock. Fitted with a cantilevered post as an assembly, the IGVs were positioned in the blanking plate. The blanking plate was then installed in the front wall of the test assembly. Scribe lines indicating the exit angle of each IGV were marked into the ends of the post attached to the IGV. Using this scribe line, the IGVs were angled to replicate the exit angles of the IGVs used in the numerical model. All other components remained unchanged from baseline and previous testing by Gannon et al. [9]. Figures 19, 20 and 21, respectively, show the fabricated IGVs in various stages of assembly into the CFTA.

Figure 19.   Assembled Inlet Guide Vanes
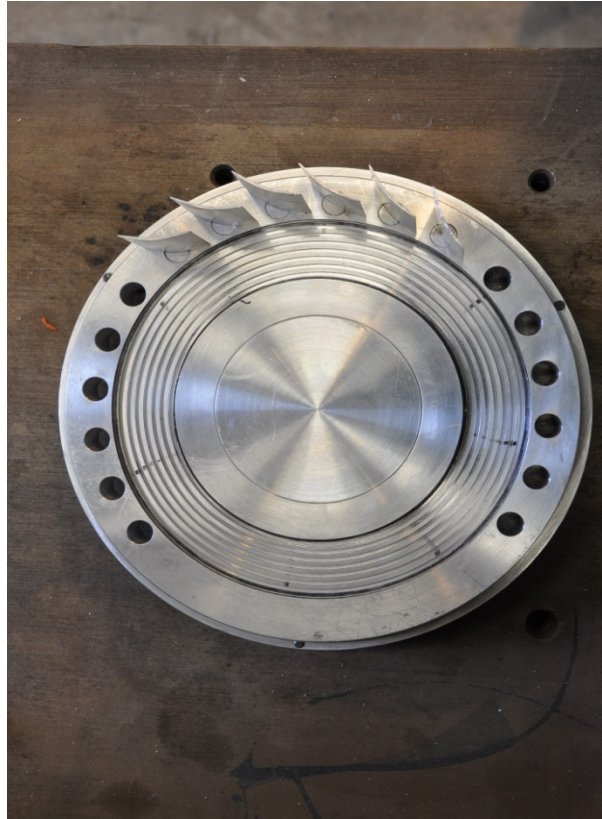
Figure 20.   Inlet Guide Vanes Installed in Blanking Plate
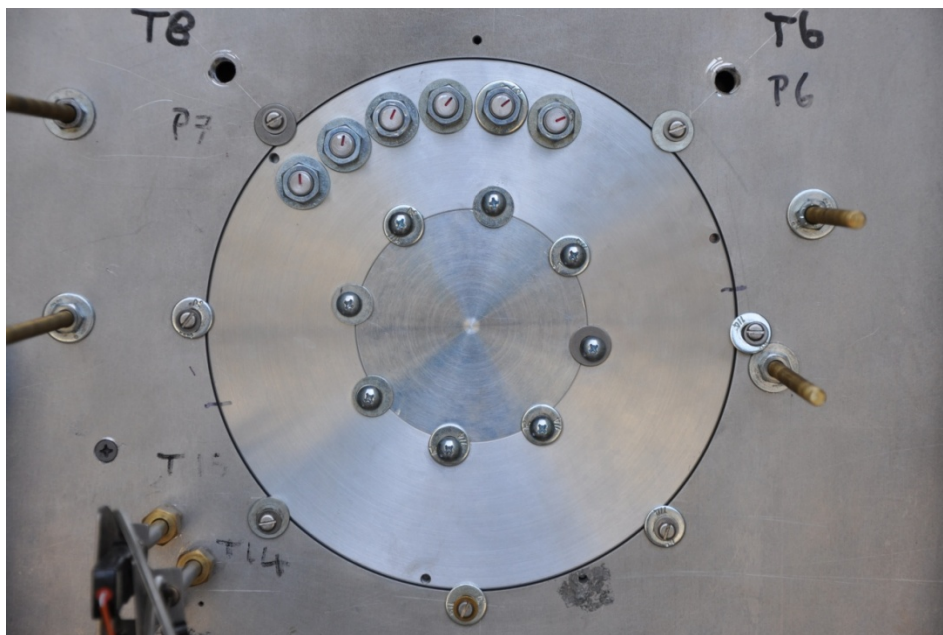
Figure 21.   Inlet Guide Vanes Installed in Blanking Plate in the CFTA Housing
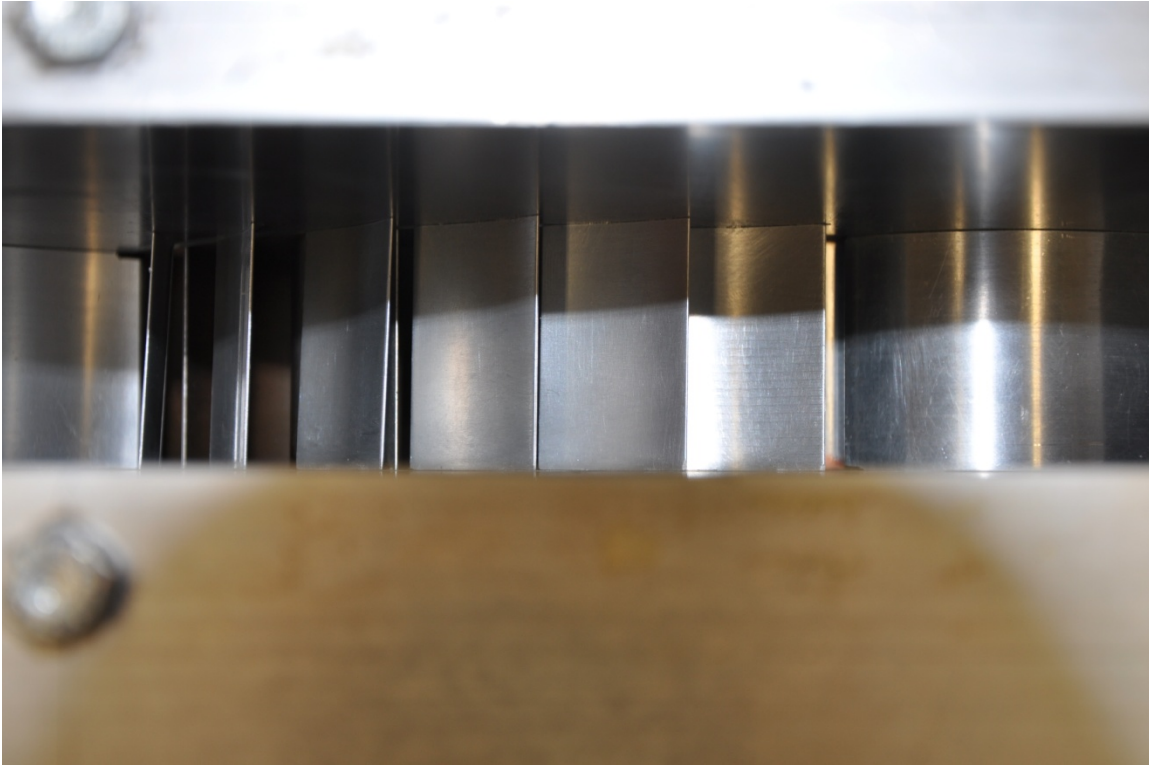
Figure 22.   Installed IGVS as Viewed from the CFF Inlet

2.   Turbine Test Rig

Motive power for the CFTA was provided by the existing Turbine Test Rig (TTR) at the Turbo Propulsion Laboratory (TPL) of the Naval Postgraduate School. The turbine itself in the TTR was driven by compressed air provided by an Allis-Chalmers 12-stage axial compressor capable of producing 10,000 cubic feet (283.17 m^3) of air at 30 psig (206.84 kPa-g). The compressor was in turn powered by a 1,250 horsepower (932.12 kW) electric motor. Air was routed from the Allis-Chalmers compressor through an air to water heat exchanger to cool the air to slightly above ambient temperature, into the test cell chamber and into the TTR, as shown in Figure 23. Additionally, an in-line oil mister provided lubrication for both the TTR turbine and the CFTA drive shaft bearing.
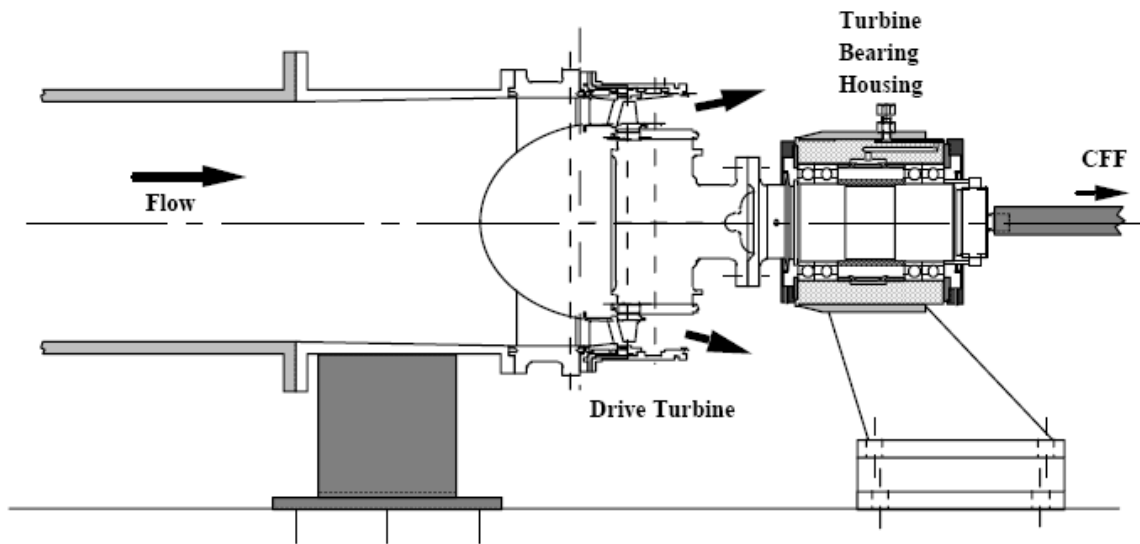
Figure 23.   Schematic of Turbine Test Rig (TTR) [From 4]

B.   CONTROL AND INSTRUMENTATION

1.   Control

Control of the TTR was executed via a remote control station.   Located outside of the TTR test cell adjacent to a window for viewing into the test cell, the remote control station was used to control air flow from the plenum chamber and into the TTR, and thus, controlled the speed of the TTR.   Speed was monitored through a once-per-revolution signal from the TTR.   Figure 24 shows the remote control station and associated monitoring characteristics.
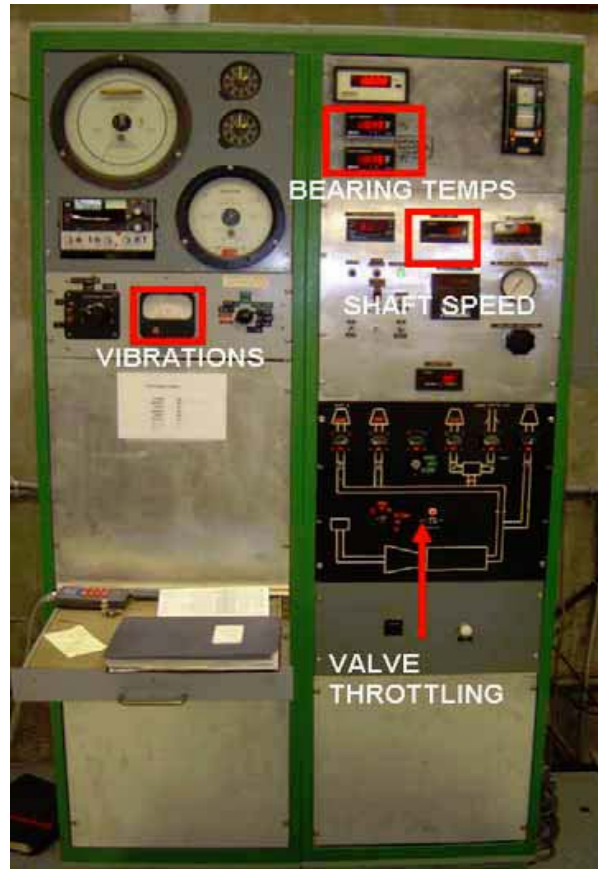
Figure 24.   TTR Remote Control Station [From 5]

2.   Instrumentation

Instrumentation for experimental investigation was similar to that used by Ulvin [7] and previous researchers at the Naval Postgraduate School [3, 4, 5, 6, 8]. Flow field properties (temperature and pressure) were measured using United Sensor Devices model USD-C-161 1/8th inch (3 mm) combination thermocouple/pressure probes and static pressure taps. Tubes from the pressure probes were routed to a 16-channel 2.5 psig (17,237 Pa) Scanivalve digital sensing array (DSA), converting mechanical pressure signals into analog electronic signals.

Three static pressure taps were used in the inlet bell mouth for determination of mass flow rate. Three combination probes were installed in the intake section at roughly the 10, 12 and 2 o'clock positions relative to the axis of rotation of the CFF. However, unlike Ulvin [7], the pressure probes at 10, 12, and 2 o'clock positions were not

32

mechanically averaged. The 10, 12, and 2 o'clock pressure probes were measured and recorded individually. The remaining instrumentation from Ulvin [7] was repeated with three combination total pressure probes and one static pressure probe installed in the exhaust portion of the CFF and a once-per-revolution counter on the TTR. All combination probes were oriented such that the pitot opening was placed at the midpoint between the front and back plates of the CFF. The pitot openings were also aligned with the anticipated flow direction for each individual location. A schematic representing the locations of the combination probes and static pressure taps was shown in Figure 6.

C.   DATA ACQUISITION

1.   Acquisition

Once the mechanical pressure signals were converted to analog electrical signals at the Scanivalve DSA, the analog signals were converted to digital within the DSA as well. The digital pressure signals as well as the thermocouple signals were then each sent to multiplexers. Downstream of the multiplexers was an HP E1326B Multimeter Adapter within a VXI mainframe connected to a Pentium based PC. The once-per-revolution signal from the TTR was routed to a counter-totalizer for RPM indication.

Software used to acquire, store and process the measured data was nearly identical to that used by Ulvin in [7]. The software program Agilent VEE was used and the graphical user interface (GUI) developed by Ulvin with three modifications. The fist modification is to account for the elimination of the mechanical averaging of the 10, 12 and 2 o'clock total pressure probes. In Ulvin's experiment, these probes were connected to a common pressure tube and in turn connected to a single port on the Scanivalve DSA [7]. For the presents study, the total pressure probes at 10, 12 and 2o'clock were each assigned their own ports and were averaged as necessary in the data acquisition software vice mechanical averaging. The remaining modifications to the data acquisition software accounted for changes in area due to the 1.5 inch (3.81 cm) span and smaller (3.25 inch vs. 6.25 inch diameter /8.25 cm and 15.88 cm respectively) inlet bell mouth used. Tables1 and 2, respectively, list the port and multiplexer channel numbers, location in the CFTA (shown in Figure 6), and data type.

Port Number	Probe	Nomenclature	Type
6	A	Pt_A	Total Pressure
8	B	Pt_B	Total Pressure
9	C	Pt_C	Total Pressure
3	10 o'clock	Pt_10	Total Pressure
4	12 o'clock	Pt_12	Total Pressure
5	2 o'clock	Pt_2	Total Pressure
2		Ps_in	Static Pressure
7		Ps_out	Static Pressure
1		P_cell	Static Pressure

Table 3.   Pressure Measurements

Multiplexer Channel	Probe	Nomenclature
13	A	Tt_A
14	B	Tt_B
15	C	Tt_C
8	10 o'clock	Tt_10
9	12 o'clock	Tt_12
6	2 o'clock	Tt_2

Table 4.   Temperature Measurements

2. Data Reduction

Using the Equations from [9] with a non-dimensionalized velocity X, the properties of the flow field and performance of the cross-flow fan were mass averaged using the following formulations:

$$X_i = \frac{v_i}{v_{i,t}} \text{ where } v_{t,i} = \sqrt{2c_p T_{t,i}} \text{ and } X_i^2 = \frac{\frac{\gamma-1}{2}M^2}{1+\frac{\gamma-1}{2}M^2} \qquad (7)$$

Where c_p is the specific heat of air at constant pressure, γ is the ratio of specific heats and M is the Mach number. Using Equation (7) and substituting into relations from [9] yielded the following relationships for temperature, pressure, and density in compressible flows:

$$\frac{T_i}{T_{t,i}} = 1 - X_i^2 \qquad (8)$$

$$\frac{P_i}{P_{t,i}} = \left(1 - X_i^2\right)^{\frac{\gamma}{\gamma-1}} \qquad (9)$$

$$\frac{\rho_i}{\rho_{t,i}} = \left(1 - X_i^2\right)^{\frac{1}{\gamma-1}} \qquad (10)$$

Manipulating the above equations to find velocity, it's non dimensional equivalent, and density in terms of static to stagnation pressure ratio and stagnation temperature yielded:

$$v_i = X_i \sqrt{2c_p T_{t,i}} = \sqrt{1 - \left(\frac{P_i}{P_{t,i}}\right)^{\frac{\gamma-1}{\gamma}}} \sqrt{2c_p T_{t,i}} \qquad (11)$$

$$X_i = \sqrt{1 - \left(\frac{P_i}{P_{t,i}}\right)^{\frac{\gamma-1}{\gamma}}} \qquad (12)$$

$$\rho_i = \frac{P_{t,i}}{RT_{t,i}} \left(1 - X_i^2\right)^{\frac{1}{1-\gamma}} \qquad (13)$$

35

Where the i subscript denotes the particular location where the property is desired, the t subscript denotes total or stagnation value, $c_p = 1004.4$ J/(kg·K), and $\gamma = 1.402$. Mass flow rate can then be determined by the following:

$$\dot{m}_i = \rho_i v_i A_i \qquad (14)$$

A_i is the area for each region where measurements occur. For the bell mouth inlet with a diameter of 3.25 inches (8.26 cm), the inlet area is 8.22958 in² (53.52098 cm²). The areas for the outlet were calculated based on the height of each probe in the exit duct and the span of the fan and exit duct of 1.5 inches (3.81 cm). The locations and corresponding heights for influence zones in the duct are shown in Figure 25 with corresponding area calculations shown in Table 5.
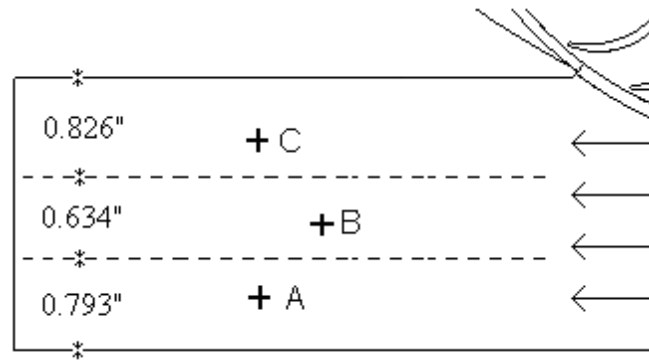
Figure 25.   Measured Heights for Zones A, B, and C in the Exit Duct

Zone	Area in², (m²)
A	1.239, (0.0007995)
B	0.951, (0.0061355)
C	1.190, (0.0007674)

Table 5.   Calculated Exit Duct Areas

Finally, the mass averaged total pressure and temperature were then obtained from the following:

$$\overline{P}_{t,out} = \frac{\dot{m}_A P_{t,out,A} + \dot{m}_B P_{t,out,B} + \dot{m}_C P_{t,out,C}}{\sum\limits_{i=A}^{C} \dot{m}_i} \qquad (15)$$

$$\overline{T}_{t,out} = \frac{\dot{m}_A T_{t,out,A} + \dot{m}_B T_{t,out,B} + \dot{m}_C T_{t,out,C}}{\sum\limits_{i=A}^{C} \dot{m}_i} \qquad (16)$$

Total pressure ratio, total temperature ratio and efficiency were then calculated according to:

$$\pi = \frac{\overline{P}_{t,out}}{\overline{P}_{t,in}} \quad (17) \qquad\qquad \tau = \frac{\overline{T}_{t,out}}{\overline{T}_{t,in}} \quad (18) \qquad\qquad \eta = \frac{\pi^{\frac{\gamma-1}{\gamma}} - 1}{\tau - 1} \quad (19)$$

Thrust was then calculated from the following assuming that u_{in} was zero:

$$F_{thrust} = \dot{m}_{in}\left(u_{out} - u_{in}\right) \qquad (20)$$

Where,

$$u_{out} = M_{out}\sqrt{\gamma R T_{out}} \qquad (21)$$

$$T_{out} = \frac{\overline{T}_{t,out}}{1 + \frac{\gamma-1}{2}M_{out}^{2}} \qquad (22)$$

$$M_{out} = \sqrt{\frac{2}{\gamma-1}\left[\left(\frac{\overline{P}_{t,out}}{P_{atm}}\right)^{\frac{\gamma}{\gamma-1}}\right]} \qquad (23)$$

And, power absorbed by the CFF was found from:

$$Power = \dot{m}_{in}\,c_p\left(\overline{T}_{t,out} - \overline{T}_{t,in}\right) \qquad (24)$$

Correction of the above parameters to standard day conditions was accomplished using the following relationships:

$$\delta = \frac{P_{t,in}}{P_{t,std}} \quad (25) \qquad \theta = \frac{T_{t,in}}{T_{t,std}} \quad (26)$$

The standard day conditions corrected values for mass flow rate, efficiency, thrust, and power absorbed was found with the following:

$$\dot{m}_{corr} = \dot{m}\frac{\sqrt{\theta}}{\delta} \quad (27) \qquad N_{corr} = \frac{N}{\sqrt{\theta}} \quad (28) \qquad F_{corr} = \frac{F}{\delta} \quad (29)$$

$$P_{corr} = \frac{P}{\delta\sqrt{\theta}} \quad (30)$$

Where $P_{t,std}$ is 101,325 Pa and $T_{t,std}$ is 288.15 K.

The above equations and correction factors were applied real time in the data acquisition software modified for the inlet bell mouth diameter and span length. Time averaged values of the data were obtained by recording five sets of data at each test point. In EXCEL, the data sets corresponding to the highest and lowest efficiency recorded for each test point was discarded and the average calculated from the remaining three data sets.

D. TEST PLANS

Initial testing of the 6D1.5L CFF was performed in a baseline or unmodified configuration in order to verify instrumentation and data acquisition software repeatability compared to previously published results on the 6 inch (15.24 cm) diameter CFF by Ulvin [7] and Gannon et al. [8]. Data runs were conducted from 3,000 rpm to 8,000 rpm in 1,000 rpm increments. At each speed, data was written to a file five times for each throttle setting until stall was approached.

Following baseline testing and validation, the 6D1.5L CFF fan housing was modified to replicate the CFD model to incorporate various combinations of six inlet guide vanes, cavities blanked off, and a horizontal vice vertical inlet arrangement. Again, test runs were conducted in 1,000 rpm increments from 3,000 to 8,000 rpm with exhaust duct throttling until stall. Table 6 identifies the various configurations tested.

Test	Housing Configuration
A	Baseline
B	No Cavities
C	Horizontal Inlet
D	No Cavities, Horizontal Inlet
E	6 IGVs, Horizontal Inlet
F	6 IGVs, No Cavities, Horizontal Inlet

Table 6.   Experimental CFF Configurations

THIS PAGE INTENTIONALLY LEFT BLANK

IV. RESULTS AND DISCUSSION

The results first presented will be from the CFD efforts because the CFD efforts drove the experiments. Since there is not a one-to-one comparison for every CFD model to an experimental configuration, comparison of the CFD models to experimental results will be discussed in the appropriate experimental section where a CFD model exists for direct comparison.

The experimental data will largely be presented as comparisons between two intermediate speed lines. Six rotational speed lines for six different experimental configurations prohibit a single graphical comparison of all configurations at all rotational speeds. Therefore, it was decide to present data only from the 4,000 and 7,000 rpm speed lines for comparison purposes.

A. INCREMENTAL CFF DESIGN CFD MODELS

As was mentioned previously in Chapter II.C, the final configuration envisioned for a possible CFF configuration was that of a 6D CFF with a horizontal inlet to facilitate incorporation into either the leading or trailing edge of an aircraft wing. Additionally, since it has been shown with previous data [4, 10] that elimination of both cavities resulted in an increase in 12D CFF efficiency over the baseline model, it was decided to numerically investigate the elimination of cavities for the 6D CFF as well. This too was investigated as part of the vision of embedding the CFF in the leading or trailing edge of an aircraft wing since elimination of the cavities would create more room for fuel storage. As much as practical, each design change of the CFF and its housing was modeled individually to determine the effects on CFF performance and resulted in the simulation plan shown in Table 1 of Chapter II.D. Table 7 shows a summary of the models and the resulting efficiencies, total temperature ratios, total pressure ratios, and mass averaged mass flow rates.

CFD Model	Efficiency	Ttot Ratio	Ptot Ratio	Mass avg. mdot out (kg/s·m)	Thrust/1m (N/m)
Baseline (Model A)	0.64	1.0064	1.01434	3.0466	138.14
Horizontal Inlet (Model B)	0.64	1.0068	1.0152	3.1726	149.73
6 IGVs, Horizontal Inlet (Model C)	0.49	1.0088	1.01523	3.1697	149.78
No Cavities, Horizontal Inlet (Model D)	0.67	1.0054	1.0127	2.9084	126.05
7 IGVs, No Cavities, Horizontal Inlet, 130 degree inlet arc, rounded casing (Model E)	0.46	1.0071	1.0115	3.0536	139.50

Table 7.   Calculated Results of Different CFF Design Configurations in ANSYS CFX

While Table 7 displays key performance characteristics of the various CFD models developed, only CFD models A through D will be discussed in detail here. CFD Model E, with a modified housing, 7 IGVs, 130 degree inlet arc, and no cavities was developed following results of Model D. However, the number of changes incorporated from Model D to Model E does not allow itself to direct comparison to any previous CFD model iteration. With Model E's obvious lack of performance improvement as shown in the data presented in Table 7, it will be discussed in Appendix C.

1.   Efficiency

In terms of efficiency, little effect was seen with the change to a horizontal inlet. However, the combination of the horizontal inlet plus the removal of the cavities yielded a higher efficiency overall compared to the base line model showing a 2.8% increase in

efficiency. This finding was consistent with the results of Cheng and Kummer [4, 10] when removing the cavities only. Finally, efficiency in the model with six inlet guide vanes suffered drastically in terms of efficiency with the results plotted in Figure 26.
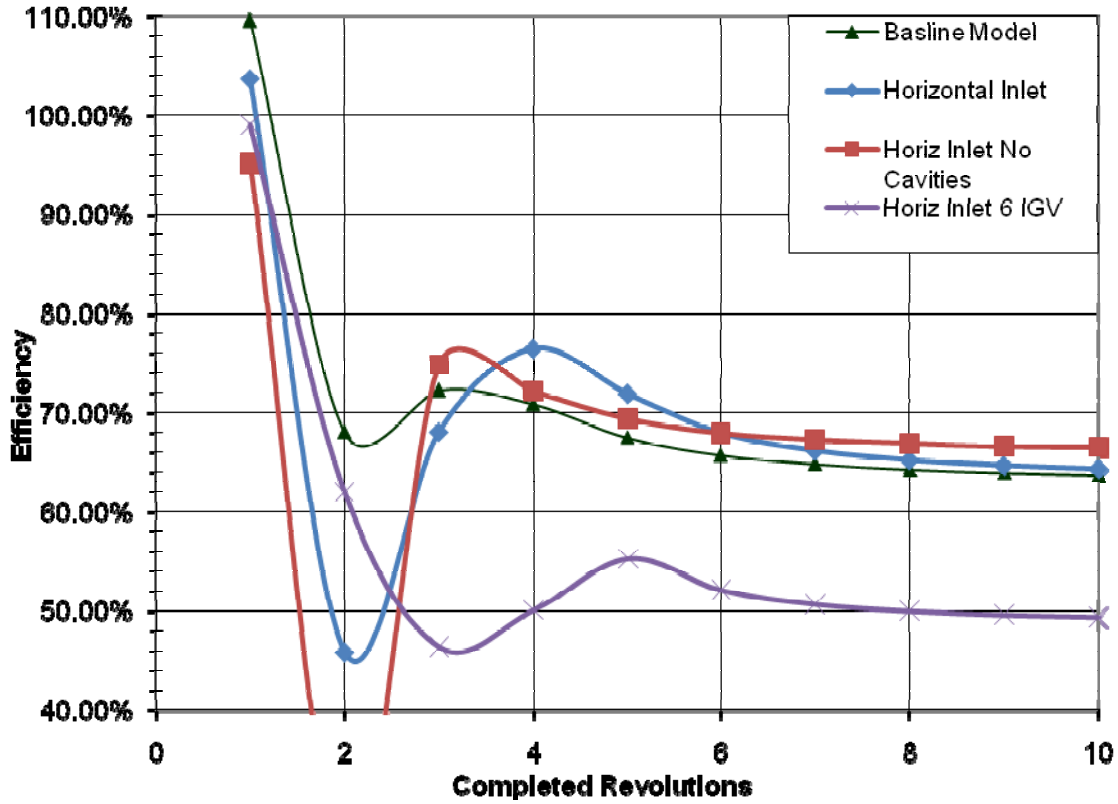
Figure 26.   CFD Model Efficiency Plots

The main contributor in the changes of calculated efficiency values can be seen in Figure 27, which plots the total temperature ratios for each of the models. Equation (19) in Chapter III.C.2 shows calculated efficiency to be a ratio of total pressure and total temperature ratios. Accordingly, the 6IGV configuration showed the highest total temperature ratios in Figure 27 with the lowest efficiency shown in Figure 26. Likewise, the lowest total temperature ratio shown in Figure 27 (horizontal inlet without cavities), resulted in the highest efficiency shown in Figure 26.
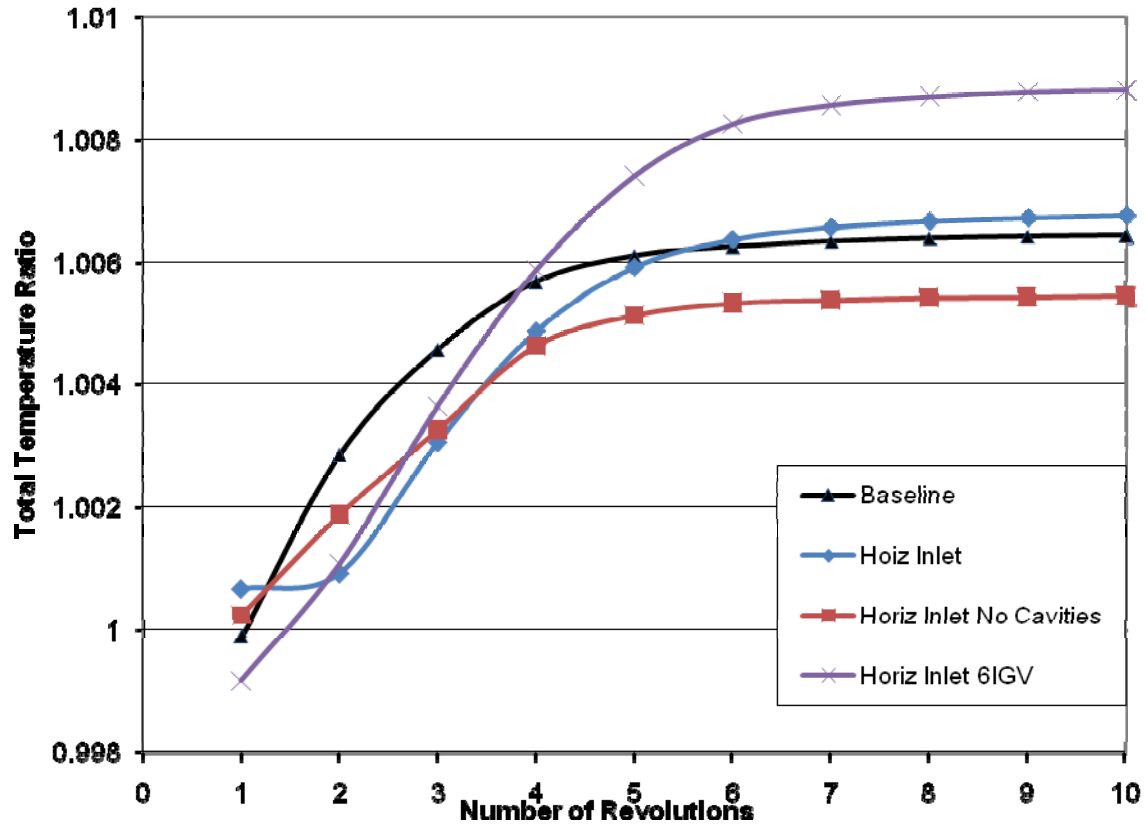
Figure 27.   CFD Model Total Temperature Plots

Additional insight into the poor efficiency of the 6IGV model may be seen by viewing the velocity vector plot. As shown in Figure 28, moving from right to left, vectors in the vicinity of the IGVs shows an increasing tendency for the IGVs to create lift and/or blockage of the flow. This can also be seen in a plot of total pressure along the fan inlet surface as shown in Figures 29 (a) and (b) comparing total pressure along the circumferential fan inlet between the base line and 6IGV models respectively. Finally, plots showing the total temperature contours (298 to 304 K) in Figures 30 (a) through (c) show the general trend that the lower efficiency models had the highest temperatures.
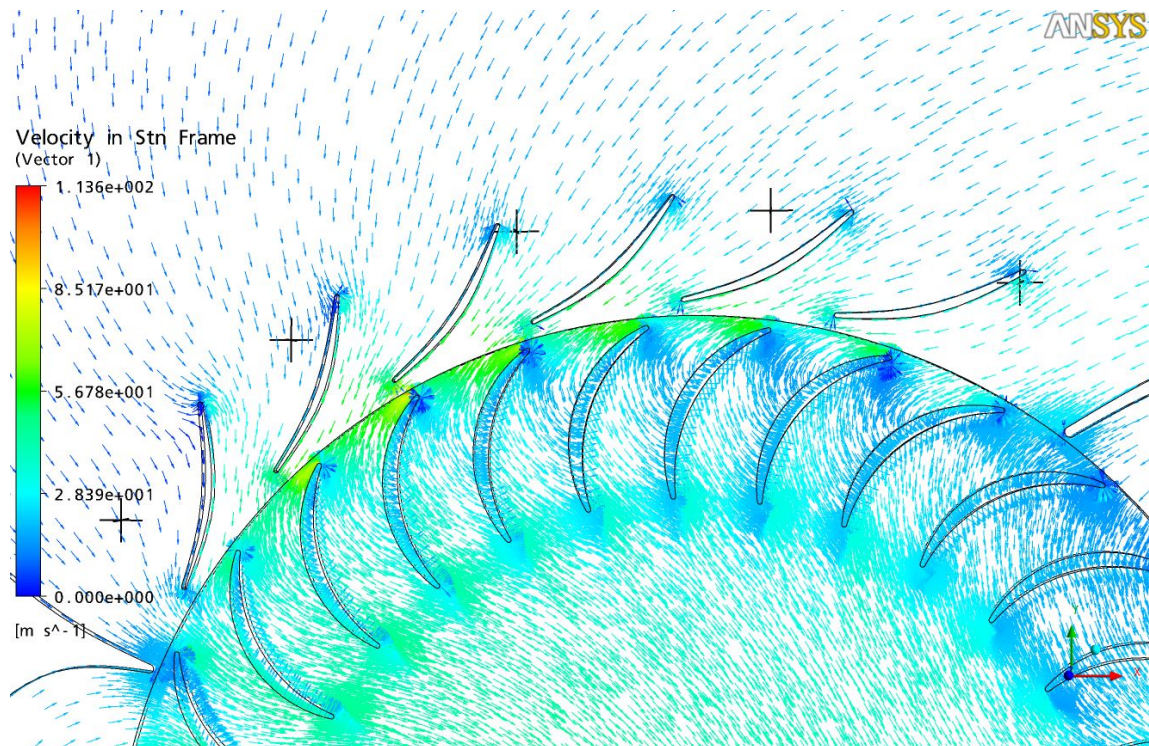
Figure 28.   Close In View of Velocity Vector Plot Near IGVS for 6IGV Model

(a)

(b)
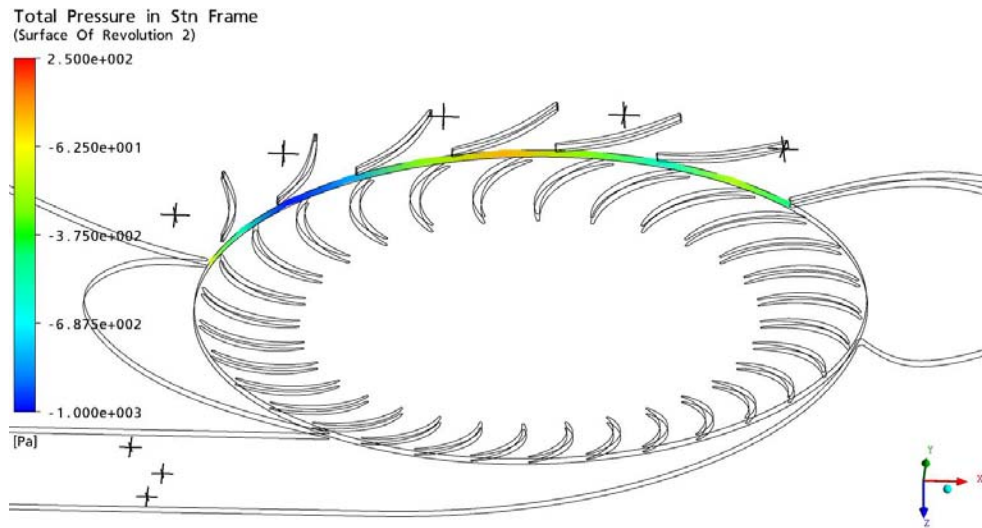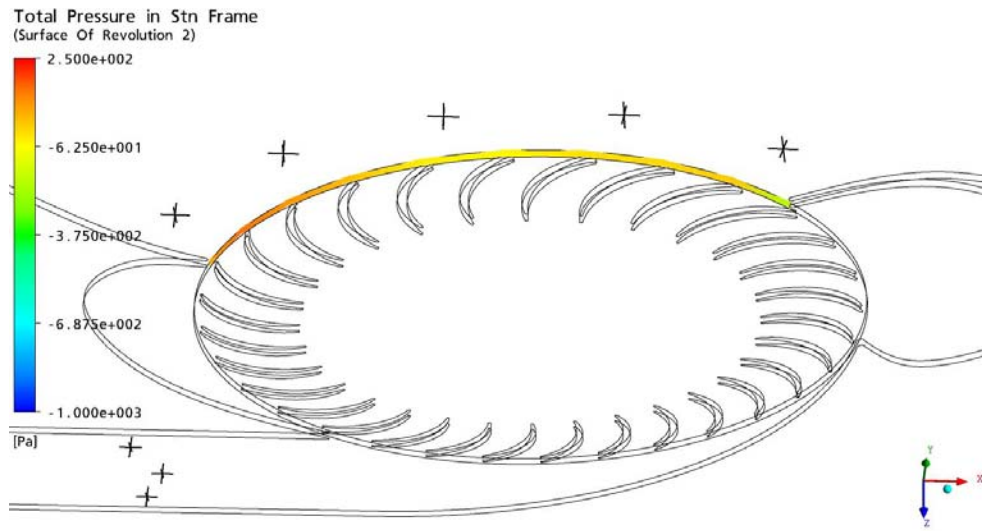
Figure 29.   Total Pressure Contour Plot along Fan Inlet Circumference for (a) Base Line Model and (b) 6IGV Model
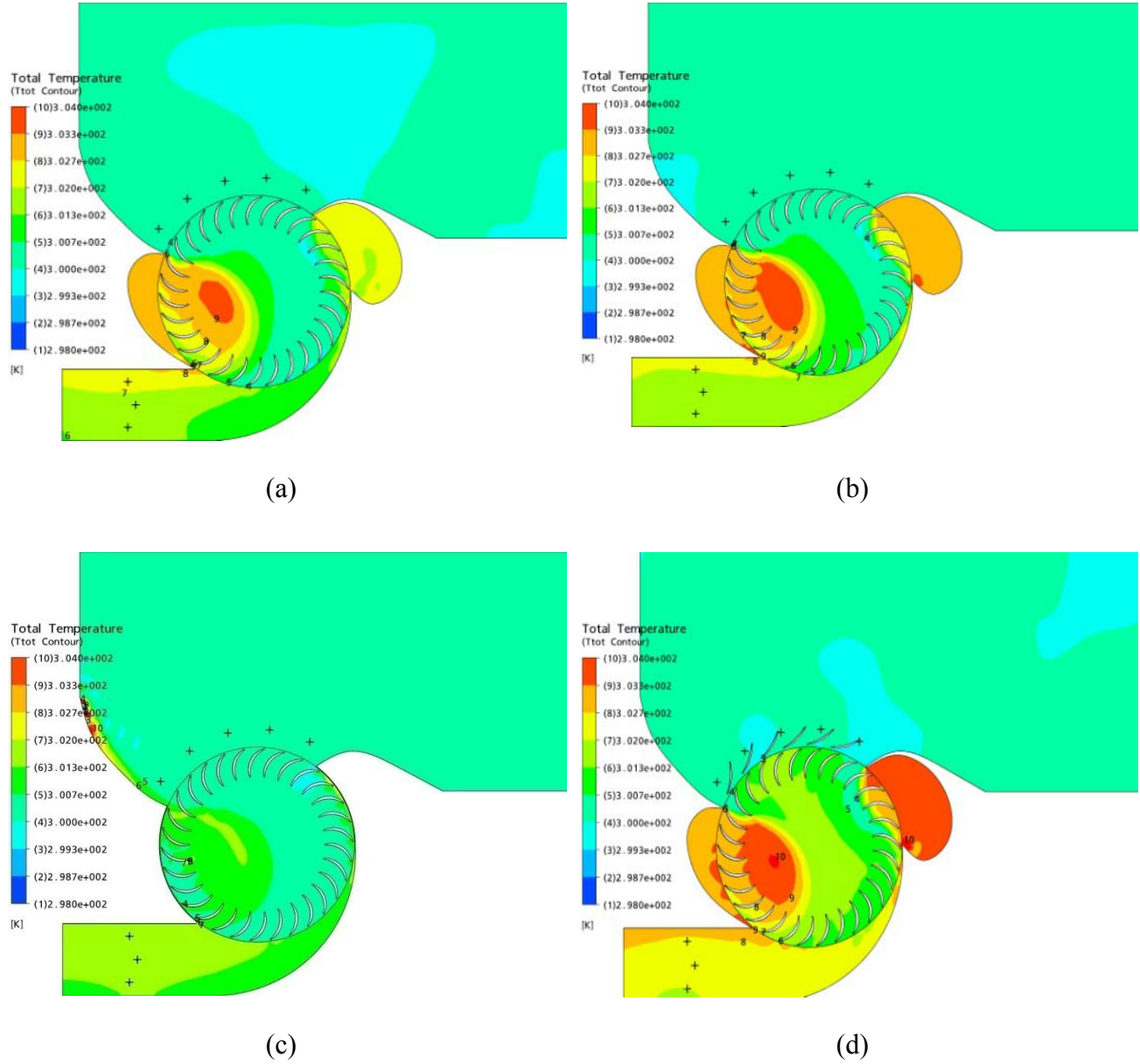
Figure 30.   Total Temperature Contours (298 to 304K) for (a) Baseline, (b) Horizontal Inlet, (c) No Cavities with Horizontal Inlet, and (d) 6IGV with Horizontal Inlet

2.   Total Pressure Ratio

The improved efficiency of the model without cavities over all other configurations, however, comes at a price. As seen in Figure 31, the model without cavities had the lowest total pressure ratio. The only individual configuration change that showed an improvement over the baseline CFD model was changing form a vertical to

47

horizontal inlet. The baseline model showed a total pressure ratio of 1.01437 while both horizontal inlet and 6IGV model with horizontal inlet showed 1.01524 and 1.01525, respectively.
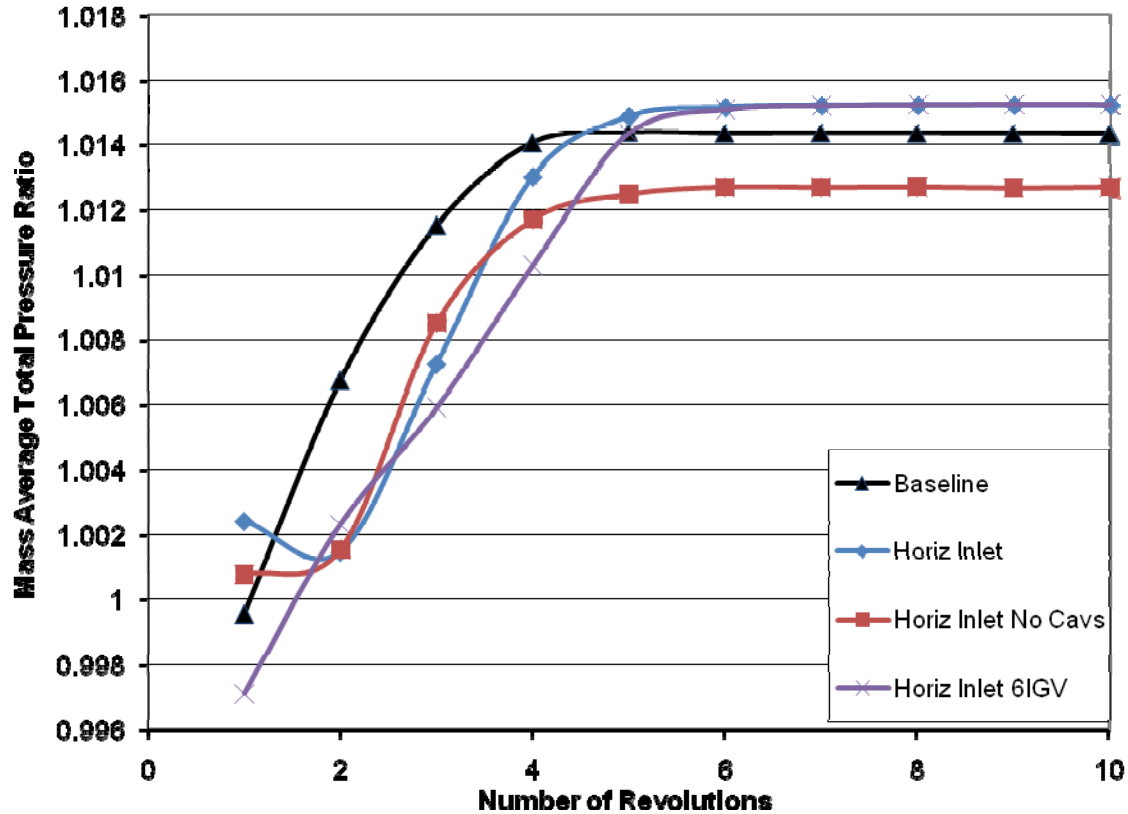
Figure 31.   CFD Model Total Pressure Ratios

As was developed earlier in Chapter I.C, the total pressure ratio is a particularly important performance parameter for a VTOL application since total pressure ratio affects thrust. Applying the theory that increased pressure ratio is possible through increasing the tangential velocity component, new probe locations on the circumferential periphery of the fan inlet arc where chosen to compare inlet velocity components and entrance angles between the various models. These new probe locations designated I through N are shown in Figure 32. These particular locations were chosen to better evaluate the effects of the IGVs on the flow as it enters the first stage of the fan. Data obtained for the various models at these locations is shown in Table 8.
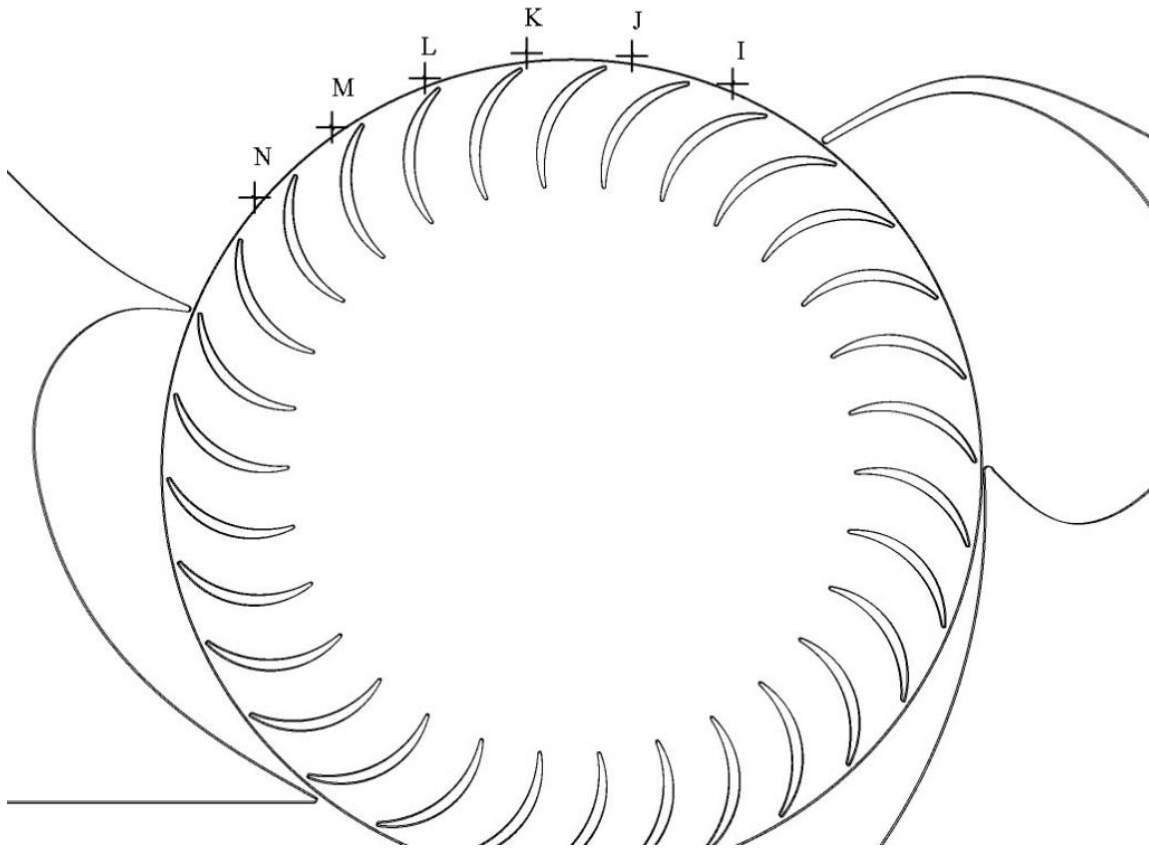
Figure 32.   Additional ANSYS CFX POST Probe Locations for Analyzing Velocity
Components Relative to Pressure Ratio

		A	B	C	D
		Baseline	**HorizInlet**	**6IGV**	**No Cavs**
Point I	**u-velocity**	-11.3800	-18.8000	-33.0500	-9.1530
	v-velocity	-10.7500	-7.5730	-5.4550	-11.1500
	angle	43.3693	21.9405	9.3723	50.6175
	Mag	15.6546	20.2680	33.4972	14.4257
Point J	**u-velocity**	-9.3910	-20.5800	-43.1200	-7.9930
	v-velocity	-13.5000	-9.0210	-11.3800	-13.4800
	angle	55.1764	23.6697	14.7841	59.3341
	Mag	16.4451	22.4703	44.5964	15.6716
Point K	**u-velocity**	-7.5470	-17.7400	-47.7100	-5.7600
	v-velocity	-15.6500	-19.9600	-28.1700	-14.9700
	angle	64.2549	48.3700	30.5594	68.9548
	Mag	17.3747	26.7041	55.4057	16.0399
Point L	**u-velocity**	-5.6970	-9.3760	-37.7200	-2.7980
	v-velocity	-20.2300	-24.6600	-46.3900	-17.0700
	angle	74.2722	69.1827	50.8852	80.6912
	Mag	21.0169	26.3823	59.7899	17.2978
Point M	**u-velocity**	2.1520	1.4320	-21.0300	3.8500
	v-velocity	-23.6800	-24.9200	-52.4700	-19.6700
	angle	-84.8073	-86.7112	68.1591	-78.9255
	Mag	23.7776	24.9611	56.5275	20.0432
Point N	**u-velocity**	12.2400	11.9800	-2.6290	10.4500
	v-velocity	-22.0700	-20.8300	-44.8300	-16.5000
	angle	-60.9873	-60.0954	86.6438	-57.6526
	Mag	25.2369	24.0293	44.9070	19.5308

Table 8.   Comparison of CFF Circumferential Fan Inlet Probe Velocity Components

Table 8 data represents the velocity components in meters per second and angles in degrees from horizontal. In the case of the positive angle quantities, a smaller angle indicates closer to horizontal flow in the negative X direction. In the case of the negative angle quantities, a smaller magnitude of the angle would indicate flow more along the horizontal positive X direction. Again, referring to the process outlined in Chapter I.C earlier, if one wanted to increase the pressure ratio by increasing the tangential velocity component of the flow in the negative x direction, then the angles shown in Table 7 corresponding to a larger pressure ratio are the ones that are closer to horizontal in the

negative x-direction. In this case, the general trends from the data in Table 8 indicated that the order of highest to lowest pressure ratio developed by the various models would be models C, B, A, and finally D (horizontal inlet was highest). Comparison of Table 7 with Figure 31 and the data listed in Table 6 shows that this is indeed the case in terms of increased pressure ratio via an increased negative tangential velocity component of the flow.

However, when viewing the velocity vector data from Table 8, Model C with 6 IGVs has tangential velocity components much closer to horizontal than Model B with just the horizontal inlet. The 6 IGV Model C also had a much higher velocity magnitude than that of the horizontal inlet Model B. Yet, the increase in pressure ratio from Model B to Model C (adding the 6 IGVs to the horizontal inlet) only yielded an increase of 0.00001974. Further inspection of Figures 33 (a) and 35 (b) shows a significant amount of flow turning as well in the 6 IGV Model C compared to the horizontal inlet, however future work in this area Cylindrical vice Cartesian coordinates may lend to better comparisons.
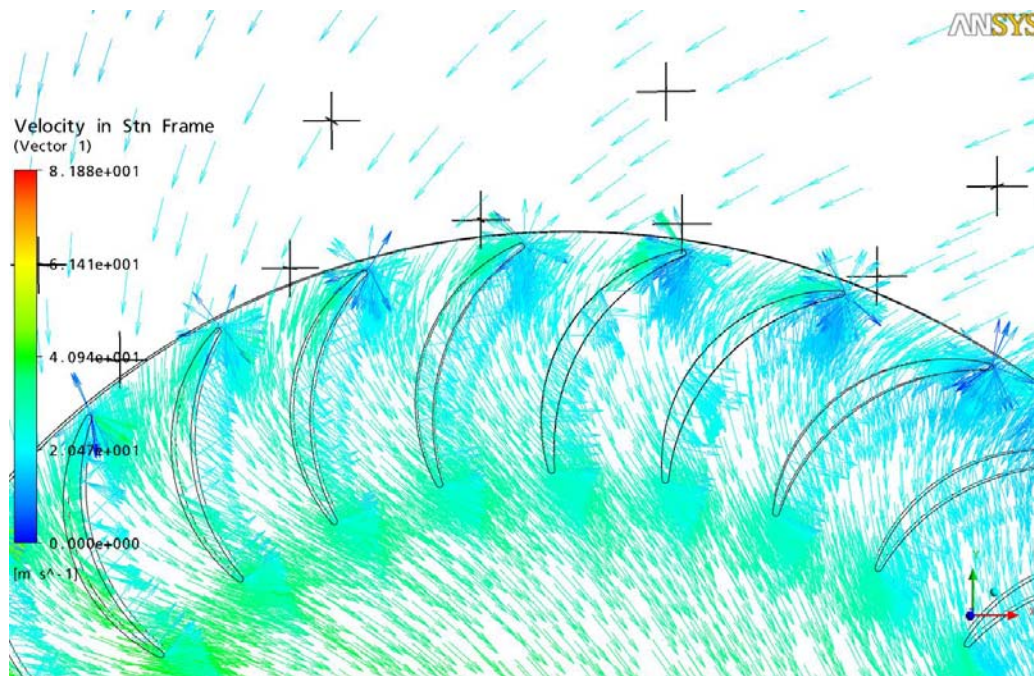
(a)
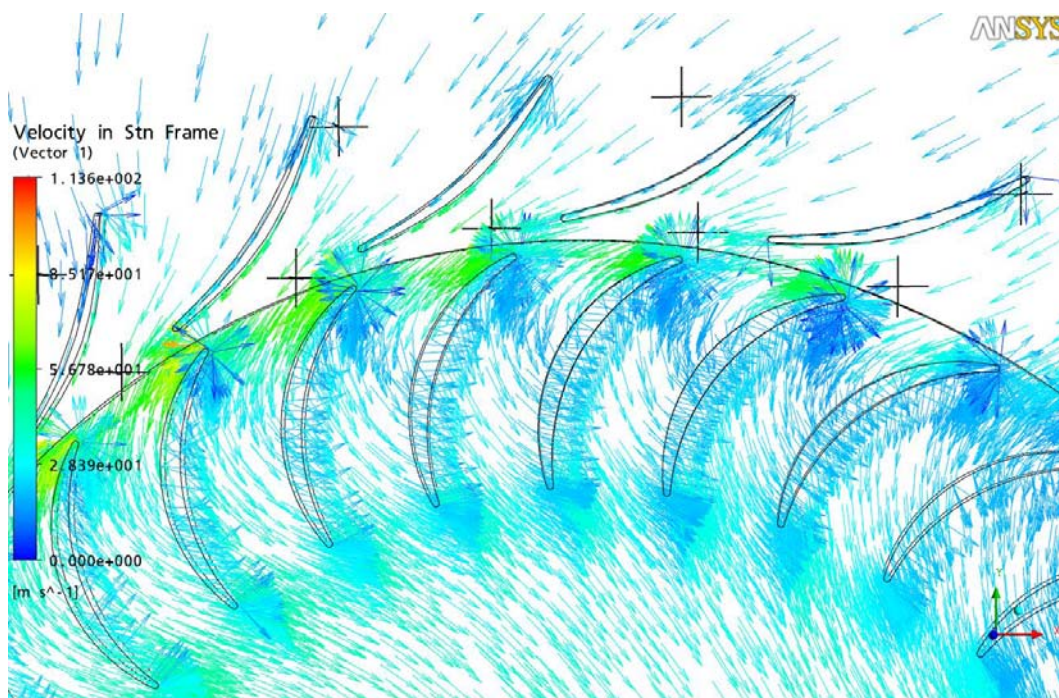
(b)

Figure 33.   (a) Horizontal Inlet and (b) 6 IGV Model Velocity Vector Plot

Inspection of the Static Entropy Contours, shown in Figures 34 (a) and (b), shows a significant increase in entropy generation in the 6 IGV Model C when compared to the horizontal inlet Model B. Figures 35 (a) and (b) show the Mach Number contours for both models as well. With the significantly increased entropy generation and higher Mach Numbers near the IGVs, as seen in the 6IGV Model C versus the horizontal inlet, Model B suggests there is a maximum amount of flow turning or change in tangential velocity component when seeking an increase in pressure ratio.
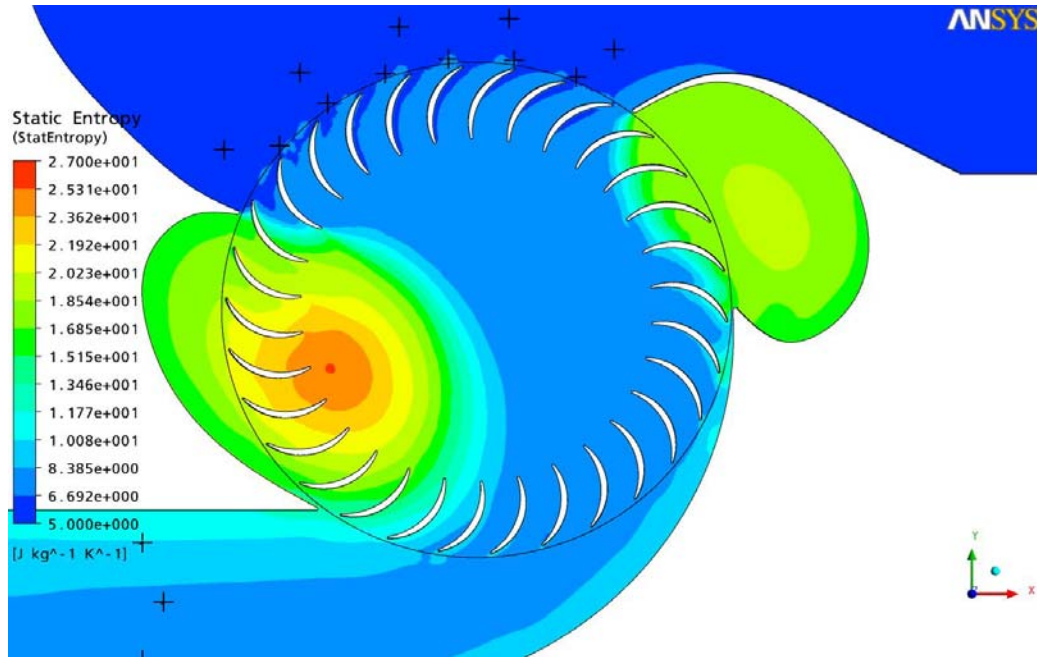
(a)
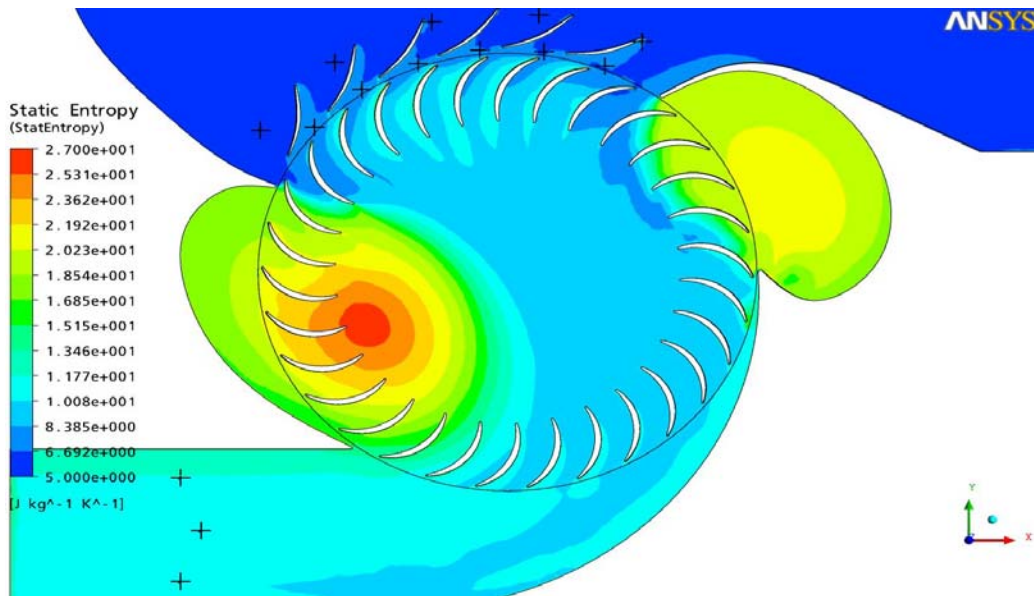
(b)

Figure 34.   Static Entropy Contours for (a) Horizontal Inlet and (b) 6 IGV CFD models
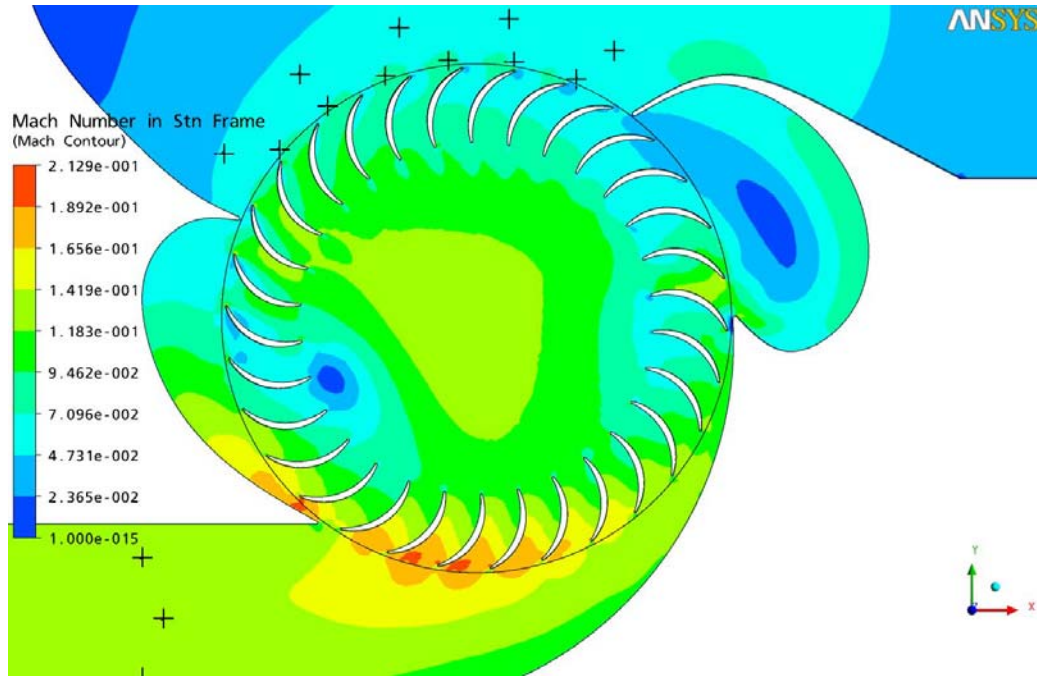
(a)
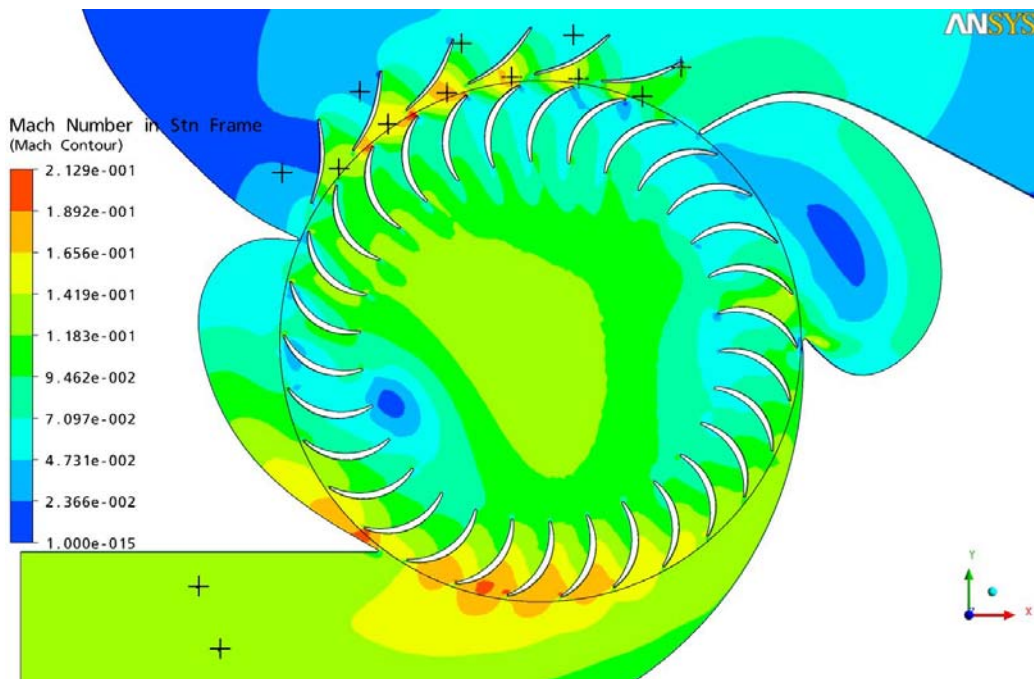
(b)

Figure 35.   Mach Number Contours for (a) Horizontal Inlet and (b) 6 IGV CFD
Models

B. BASELINE EXPERIMENTAL RESULTS

The base line model used for experimentation in [9] with many of the same components used in [7] was reassembled to verify previous data as well as new instrumentation. A new pressure transducer DSA was used, which had a range of up to 2.5 PSID (17236.89 Pa-Differential). This lower differential pressure range provided more sensitivity for the pressure readings in the flow field than in previous experiments. Figure 36 shows a compressor efficiency map with efficiency plotted versus various corrected mass flow rates normalized to a one-meter length span for various fan speeds.
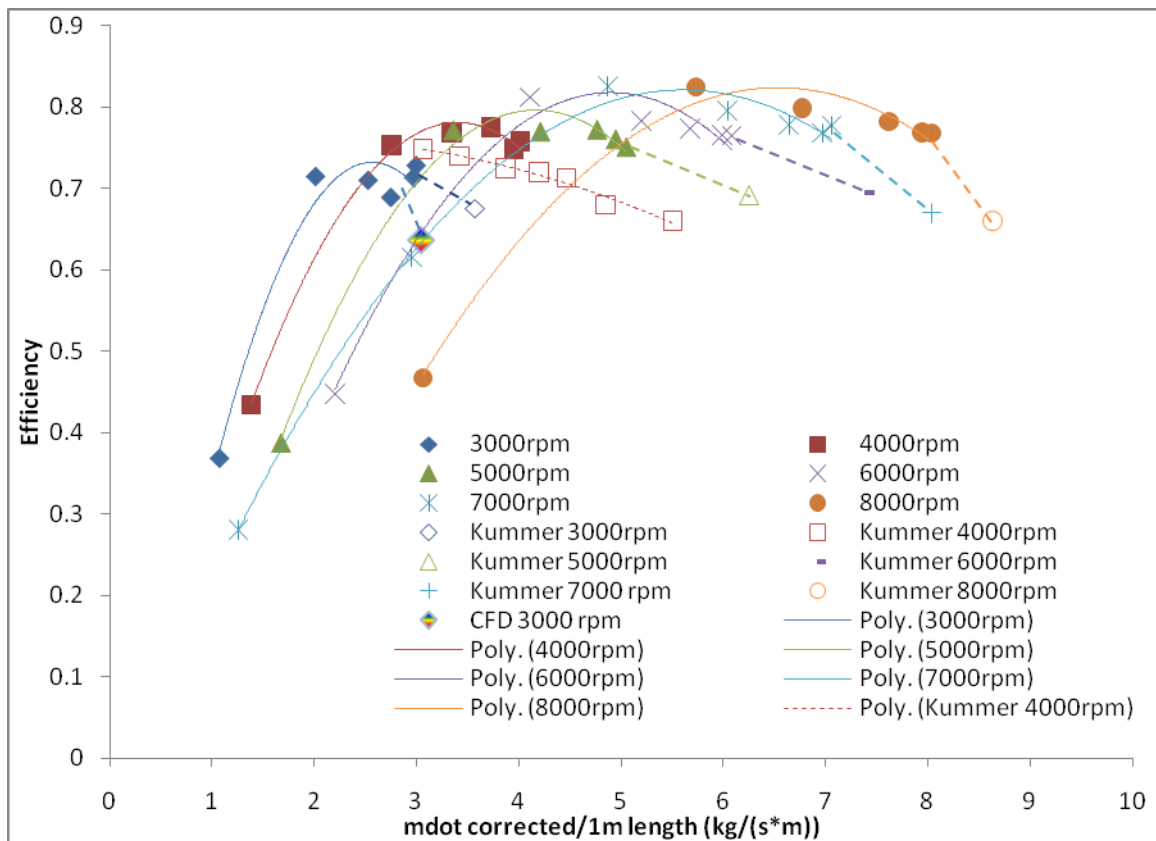
Figure 36.   Compressor Map for 6D1.5L Baseline CFF, with data extrapolated and scaled [From 10]

Comparison of Figure 37 with the previously presented Figure 11 from [7] shows agreeable trends in the data recorded; however, it should be noted that trend lines used in Figure 11 use 3rd and 4th order polynomials while Figure 21 uses 2nd order polynomials. For further comparison, Figure 21 also includes data extrapolated by hand from plots by Kummer in [10] and scaled accordingly from a 12D fan to a 6D fan using scaling laws presented by Gannon et al. in [8]. Considering the probable errors in extrapolating data by hand from Kummer's plots, the data also agrees favorably with the newer experimental data for the 6D1.5L CFF.

Due to the large mesh size of the CFD model, throttling studies were not carried out on the CFD model and, therefore, only one data point at unrestricted outlet flow and 3000 rpm exists for comparison. Using the same methodology of calculating efficiency based on mass-averaged total-temperature and total-pressure ratios from data obtained via probe measurements, the CFD baseline model at 3000 rpm yielded a calculated efficiency of 63.7% at a mass flow rate of 3.046 kg/(s·m). The experimental data yielded an efficiency of 72.8% at a mass flow rate of 2.994 kg/(s·m) at 3,000 rpm and no throttling.

C.   COMPARISON OF EXPERIMENTAL CONFIGURATIONS

1.   Efficiency

Efficiency calculations for the various configurations showed results similar to that of the CFD models in that the configurations with inlet guide vanes suffered considerably in terms of efficiency. At 3,000 rpm and open throttle, the CFD model predicted nearly a 15% reduction in efficiency by application of the IGVs. Using the data in Table 7, the CFD model predicted an efficiency of 49.38% at a corrected mass flow rate of 3.1697 kg/(s·m). Experimentally, the 6 IGV configuration returned an efficiency of 49.14% at a corrected mass flow rate of 2.6980 kg/(s·m). Both values were at 3,000 rpm.

Rearranging the inlet from vertical to horizontal appeared to have little effect on efficiency, again confirming the findings of the CFD models. However, the CFD model did predict about a 2% increase in efficiency at 3,000 rpm when the cavities were either removed or blanked off. The ability to confirm this was mixed based upon the

57

experimental results. Figure 37 shows the effects of blanking the cavities off in the CFTA at 4,000 and 7,000 rpm. As seen in Figure 37, efficiency at higher mass flow rates is higher for the baseline configuration. When mass flow rates are decreased to roughly 66% of the open throttle condition, the configurations with cavities blanked off began to operate more efficiently than the baseline model. It should be noted that the results plotted in Figure 37 compare the baseline configuration with vertical inlet to cavities blanked with vertical inlet. However, the effects on efficiency were about the same in the case of horizontal inlet as well as the case with the addition of inlet guide vanes. Finally, Figures 38 and 39 show efficiency of all configurations tested at 4,000 and 7,000 rpm.
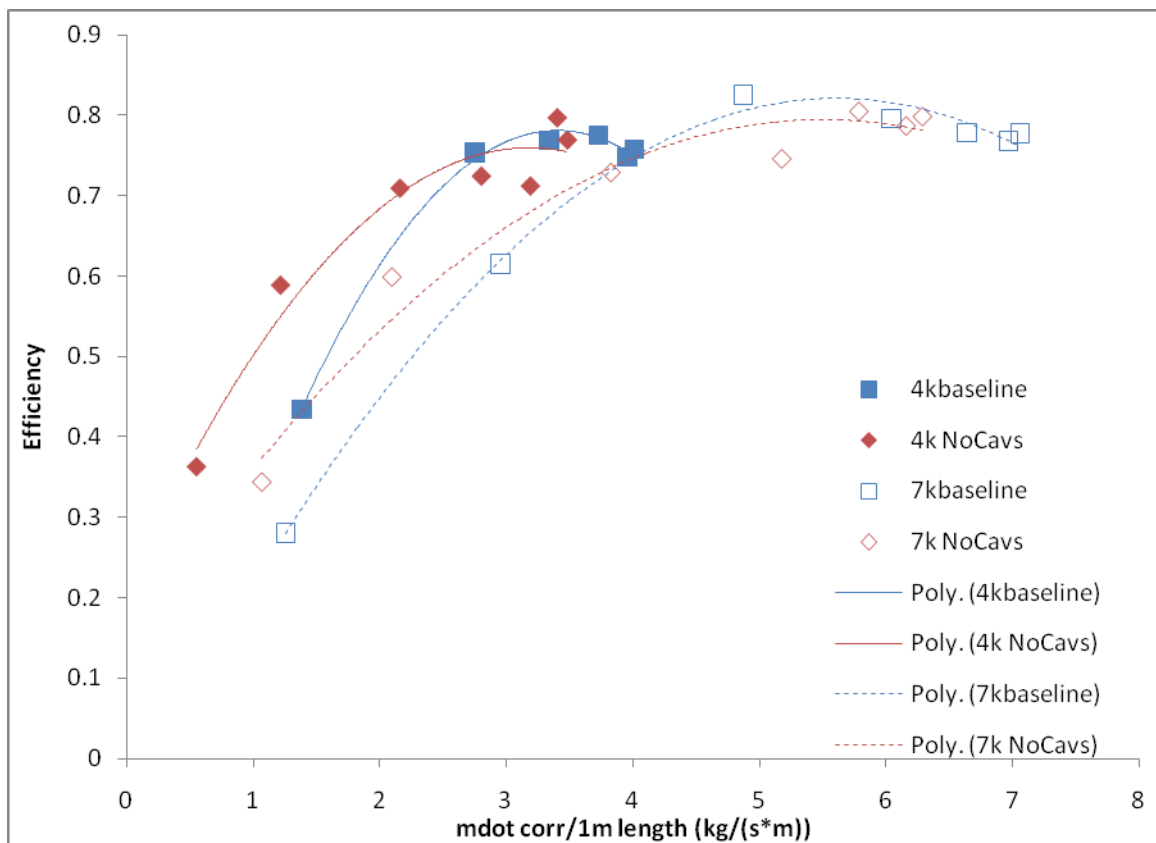
Figure 37.   Cavity Removal Effect on Efficiency at 4,000 and 7,000 rpm
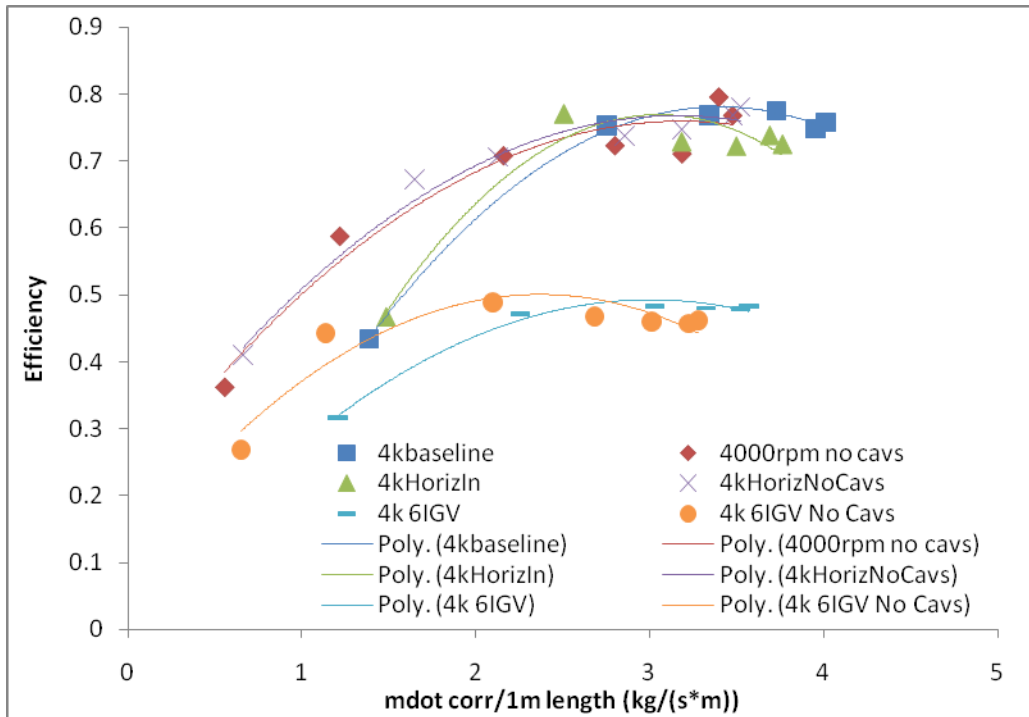
Figure 38.   Efficiency for all Experimental Configurations at 4,000 rpm
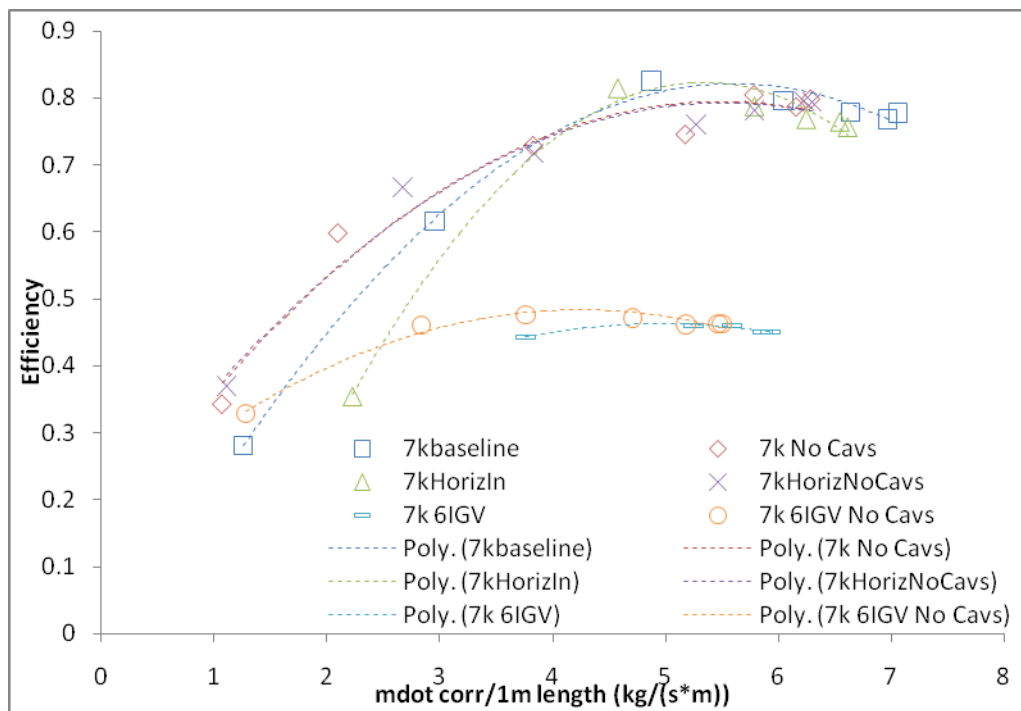
Figure 39.   Efficiency for all Experimental Configurations at 7,000 rpm

59

2. Total Pressure Ratio

In terms of total pressure ratio, the CFD model predicted a slight increase in total pressure ratio when IGVs were applied to the model. Using results from Table 7, the total pressure ratio of the CFD model with IGVs increased for the horizontal inlet model from 1.0152 to 1.0153 at 3,000 rpm and not throttling. Experimental results at 3,000 rpm with an open throttle yielded pressure ratios of 1.0132 and 1.0128 for the horizontal inlet and the 6 IGV with horizontal inlet experimental configurations. As seen in Figure 40, the degradation of total pressure ratio due to the addition of inlet guide vanes becomes more significant at higher rotational speeds.
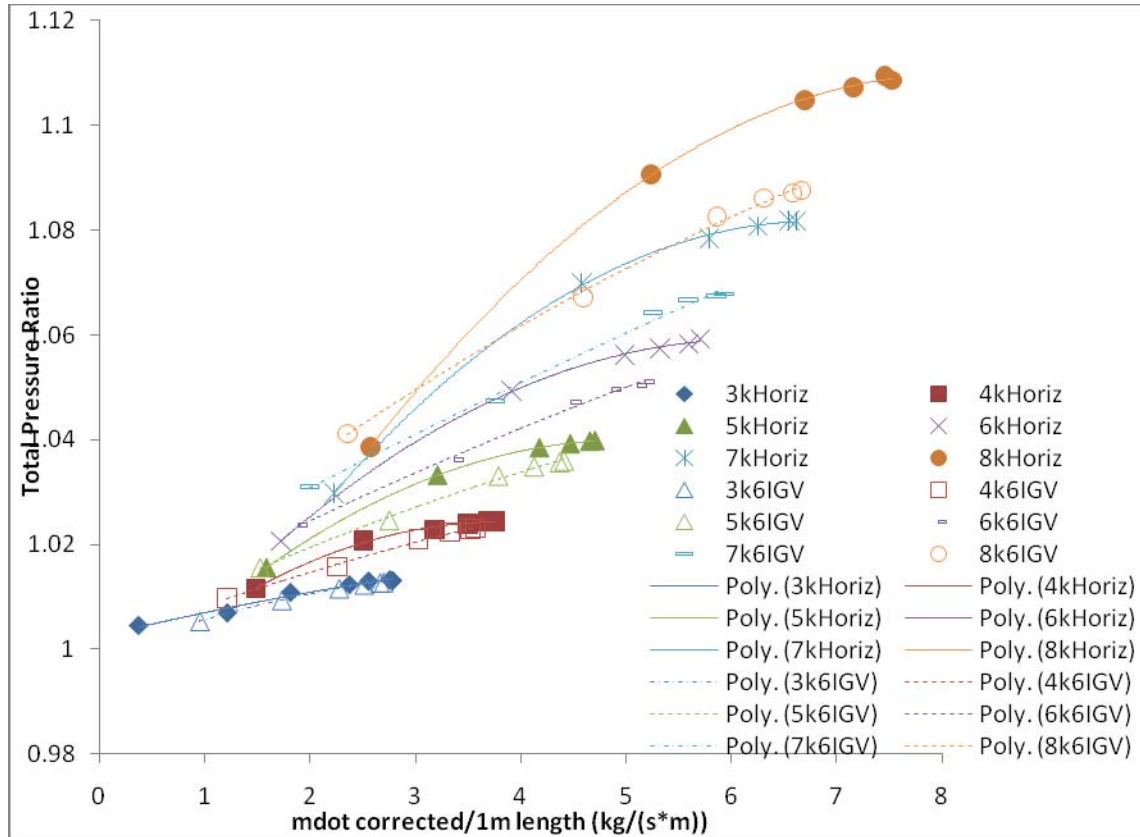
Figure 40.   Total Pressure Ratio Comparison between the Horizontal Inlet and 6 IGV with Horizontal Inlet Experimental Configurations from 3,000 to 8,000 rpm

Additionally, in all experimental configurations, the application of inlet guide vanes reduced the total pressure ratio except for the cases with the cavities blocked off under throttling. Figures 41 and 42 show a slight increase in total pressure ratio when IGVS are added to the configurations without cavities and the flow is throttled at 4,000 and 7,000 rpm, respectively.
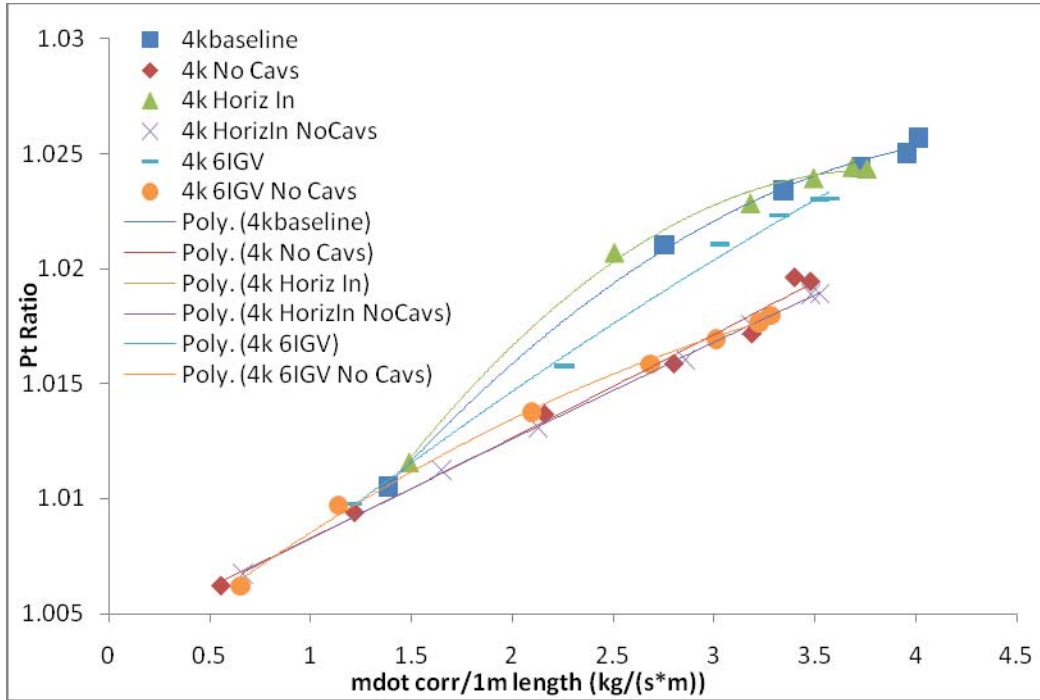
Figure 41.   Total Pressure Ratio for all Experimental Configurations at 4,000 rpm
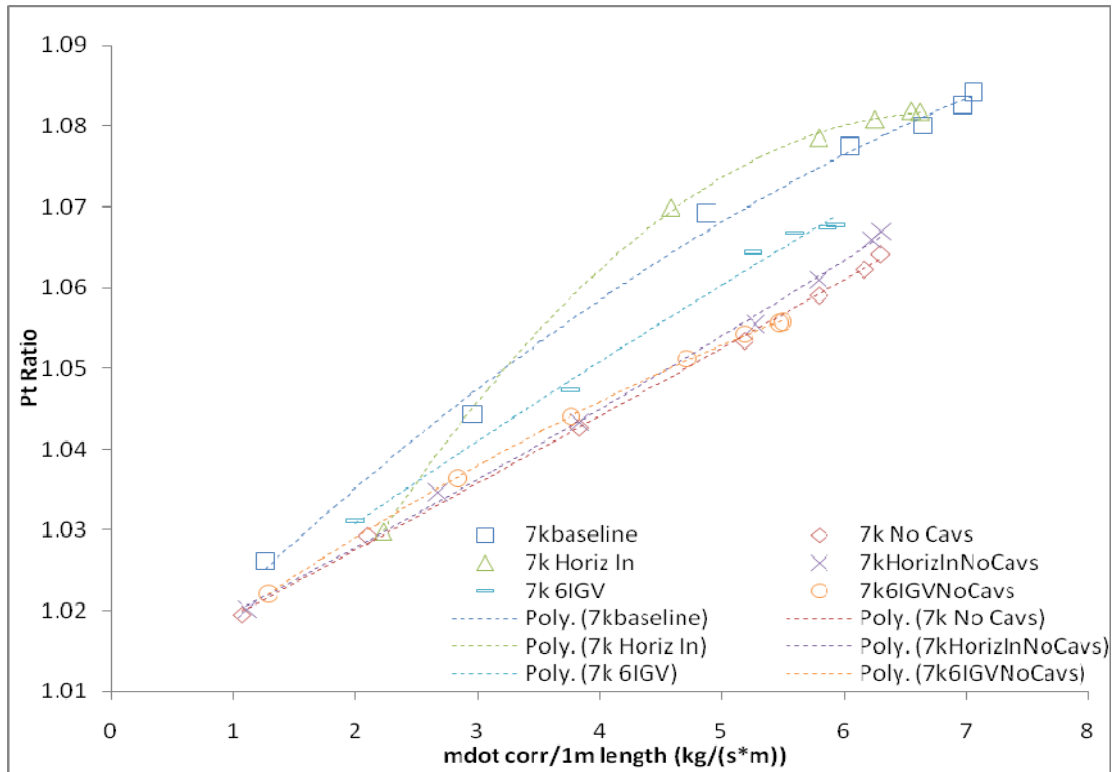
Figure 42.   Total Pressure Ratio for all Experimental Configurations at 7,000 rpm

Further investigation into the results of Figures 41 and 42 show that one experimental configuration did show an increase in total pressure ratio. The horizontal inlet showed an increase in total pressure both in the CFD model as well as experimentally. From Table 7, the CFD model showed an increase over baseline from 1.0144 at a corrected mass flow rate of 3.0466 kg/(s·m) to 1.0152 at a corrected mass flow rate of 3.1726 kg/(s·m) at 3000 rpm and no throttling. The baseline experimental configuration at 3,000 rpm and an open throttle yielded a total pressure ratio of 1.0137 at a corrected mass flow rate of 2.9936 kg/(s·m). The horizontal inlet configuration yielded 1.0132 at a corrected mass flow rate of 2.4878 kg/(s·m). Thus, the CFD and experimental results do not compare favorably in the case of open throttle conditions. However, under all throttling conditions for the experimental configuration, the general trend was that the horizontal inlet led to an overall increase in total pressure ratio. This is illustrated in Figure 43.

62
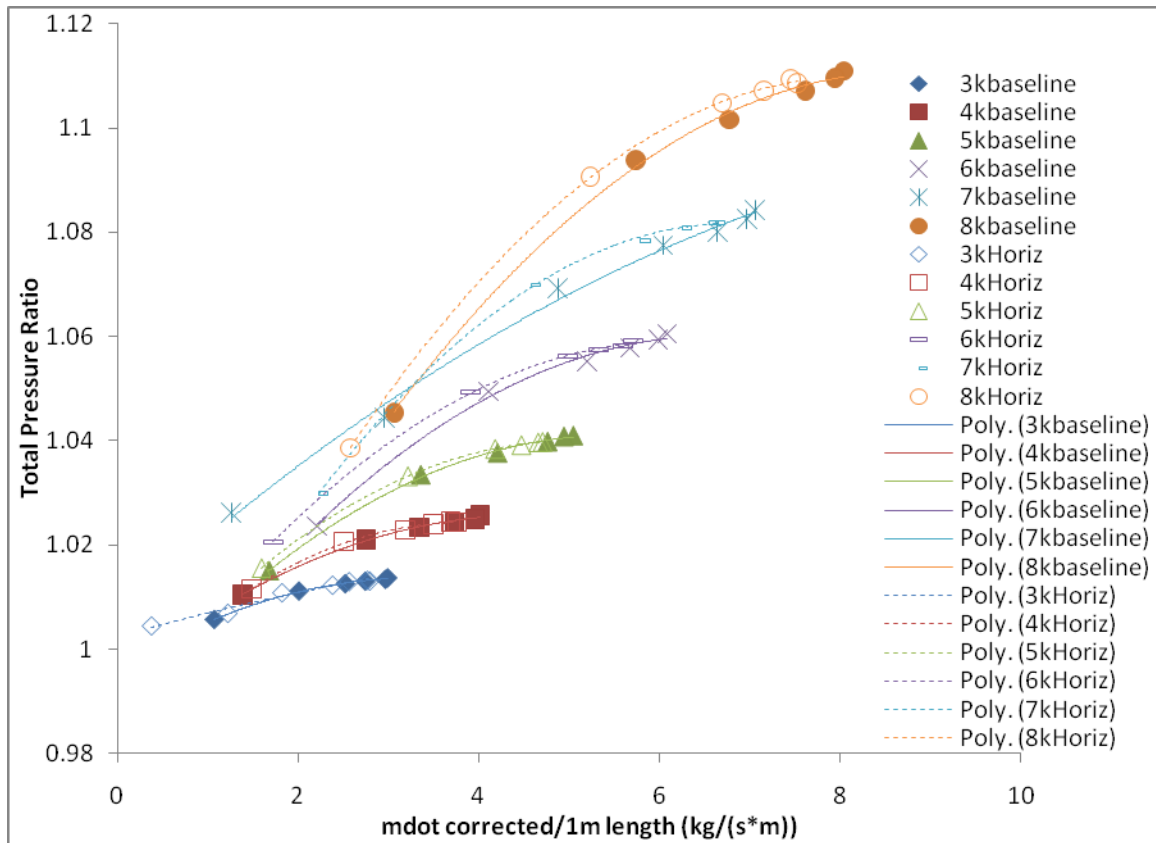
Figure 43.   Total Pressure Ratio Comparison, Experimental Baseline to Horizontal
Inlet Configurations, 3,000 to 8,000 rpm

3.   Specific Thrust

Specific thrust, in this case the amount of thrust force developed (Newtons) per unit of input power (Watts) showed perhaps the most interesting behavior of all the performance parameters. In all experimental configurations for which the cavities were blocked off, the CFF changed behavior in between 5,000 and 6,000 rpm. At speeds of 5000 rpm and lower, the CFF's response to throttling in terms of specific thrust was the same as all other models. That is specific thrust tended to increase from the value at open throttle conditions to some maximum value and then decrease as the mass flow rate was further decreased by throttling. However, at speed of 6,000 rpm and greater, all CFF configurations with the cavities blanked off did not exhibit this behavior. Specific thrust continued to increase until stall conditions were achieved. From 6,000 to 8,000 rpm,

experimental configurations in which the cavities were not blanked off continued to exhibit the behavior of reaching a maximum value and then decreasing as the mass flow rate was reduced by throttling the exhaust duct.

At speeds of 5,000 rpm and lower, experimental configurations in which the cavities were blocked off showed higher values of specific thrust over configurations with the cavities open. At speeds of 6,000 rpm and higher, configurations with the cavities blocked off had a lower specific thrust than similar configurations with the cavities open. Figures 44 and 45 shows this phenomenon for all configurations tested at 4,000 and 7,000 rpm, respectively.
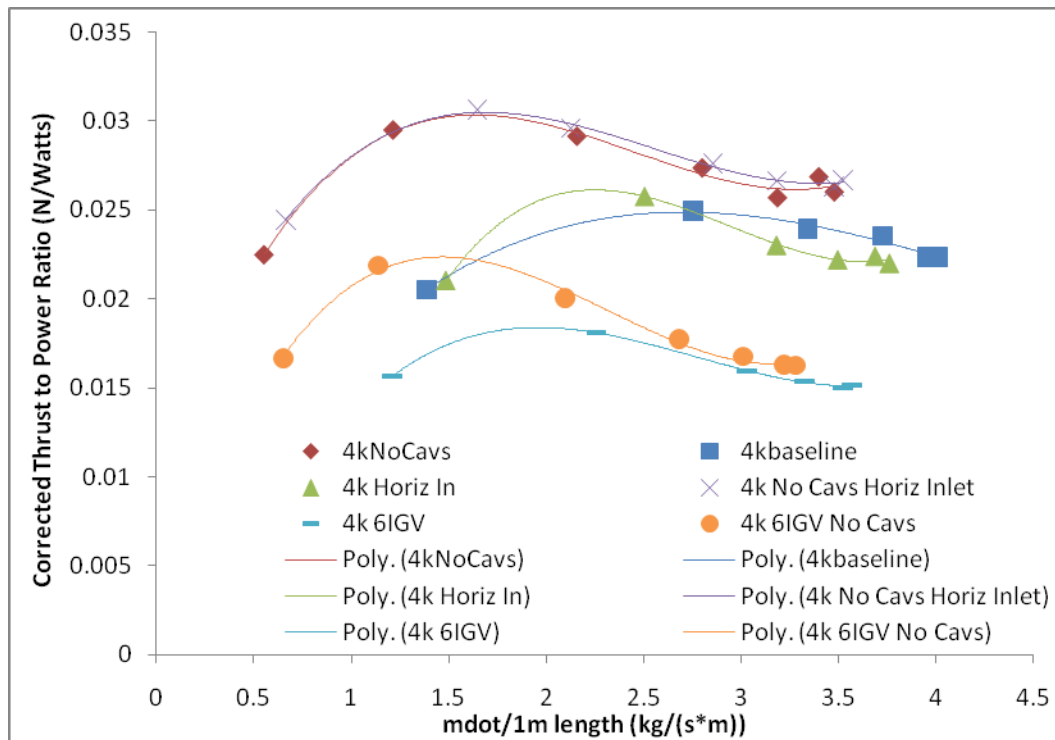
Figure 44.   Specific Thrust for all Experimental Configurations at 4,000 rpm
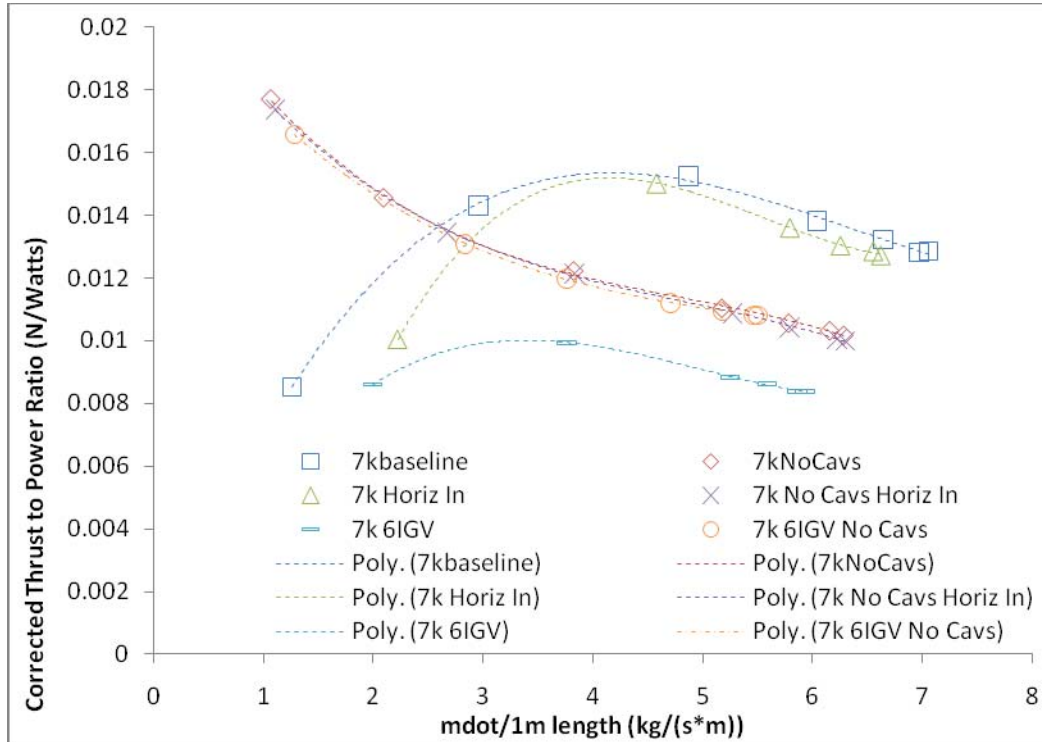
Figure 45.   Specific Thrust for all Experimental Configurations at 7,000 rpm

4.   Thrust per Unit Length

In terms of thrust developed per unit length of the CFF span, there was no significant improvement over the baseline model. Moving from a vertical to horizontal inlet did produce an increase in thrust per until length of span. However, this increase was not overly significant. On the contrary, any experimental configuration in which the cavities were blocked off did show more of a marked decrease in thrust per unit length span as well as a lower overall mass flow rate for the same throttle setting. Figures 46 and 47 show the corrected thrust per meter length of span for all experimental configurations at 4,000 and 7,000 rpm, respectively.
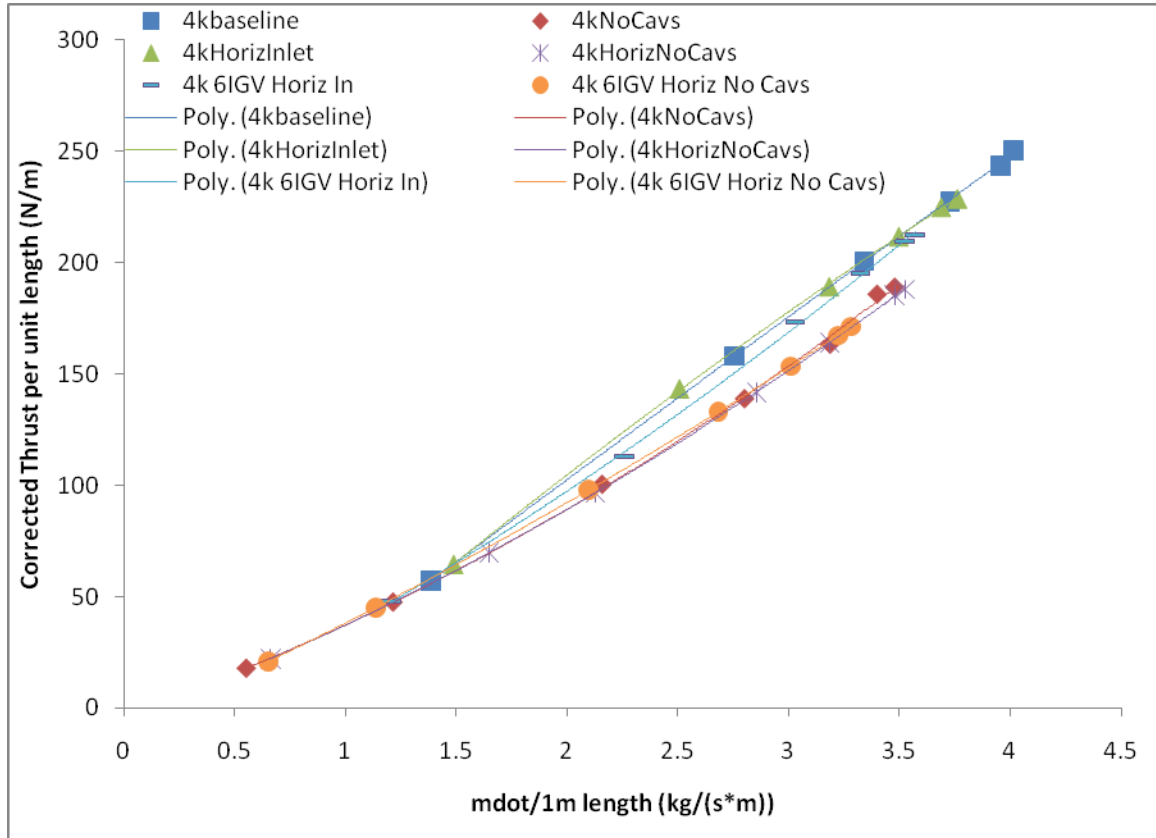
Figure 46.   Thrust per Unit Length Span for all Experimental Configurations at 4,000 rpm
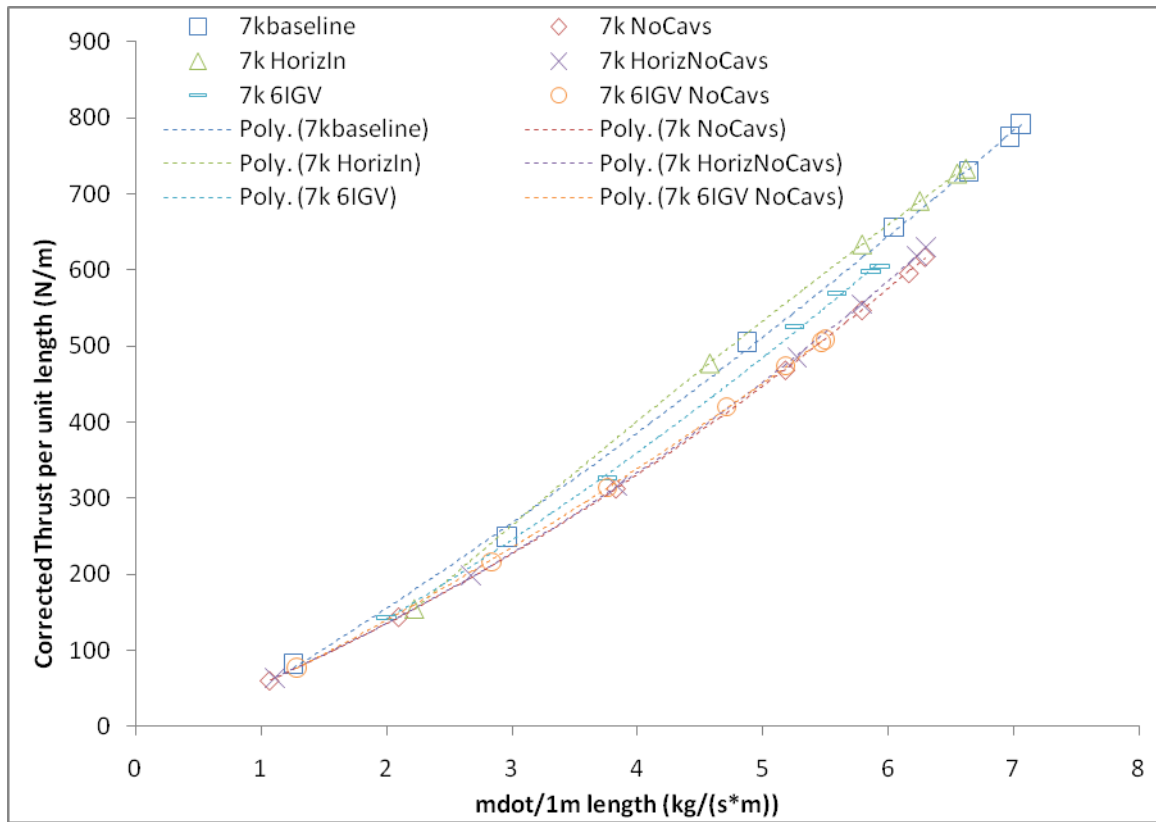
Figure 47.   Thrust per Unit Length Span for all Experimental Configurations at 7,000 rpm

THIS PAGE INTENTIONALLY LEFT BLANK

V. CONCLUSIONS

The particular inlet guide vane configuration modeled in ANSYS CFX, and then tested experimentally, did not have the desired end result of increasing thrust output of the cross-flow fan. The IGV configuration modeled and tested did, however, produce a dramatic increase in the net change of tangential velocity components of the flow as it entered the first stage blade region. Due to the nozzle effect of the IGV configuration, the overall velocity magnitude of flow field as it entered the first stage blades was increased considerably as well. Both the increase in the tangential component and magnitude of the velocity entering the first stage occurred when compared to both the baseline model and the horizontal inlet model.

However, modeling and experimental results of the horizontal inlet configurations showed an increase in tangential velocity component, pressure ratio, and thrust (under most throttling and speed conditions for the experiment) when compared to the baseline configuration. The increase in tangential velocity components in the horizontal inlet CFD model was about half that of the increase seen in the 6 IGV model over baseline. Yet, the horizontal inlet experimental configuration showed an increase in thrust while the 6 IGV configuration with a horizontal inlet showed a slight decrease in thrust when compared to baseline. This suggests that there is either an optimum value of tangential velocity components that lies between the horizontal configuration and the 6 IGV configuration, and/or that an IGV configuration with much lower induced losses is needed in order to yield increased thrust output with the application of inlet guide vanes.

THIS PAGE INTENTIONALLY LEFT BLANK

VI.   RECOMMENDATIONS

Further study on inlet, outlet and overall CFF housing configurations should be conducted. Assuming a 2-D mesh for the fan region can be incorporated into the overall computational mesh, the use of solid modeling software, such as SOLIDWORKS, to develop geometries for export into ANSYS WORKBENCH and ANSYS CFX should provide a relatively easy means of developing design variations to conduct parametric design studies of the CFF. With the incorporation of a 2-D mesh for the fan region, computational times should decrease drastically from the one day per revolution of computational times for the baseline model (computational times observed for more complex geometries were sometimes two days or more per revolution).

Parametric studies of inlet, outlet and overall housing design configurations should be made with a focus of allowing the CFF to be operated over a range of speeds. The inlet, outlet and housing should be designed such that variation of engine speed can provide an operating line as shown in Figure 48. Such an operating line would allow an operator to increase rotational speed as desired for higher thrust and to decrease rotational speed when desired for cruise type conditions when less thrust is needed (forward flight for a fan in wing concept) and economy is more important. Additionally, future research should focus on the operating regions where specific thrust is at or near maximum value for a particular rotational speed.
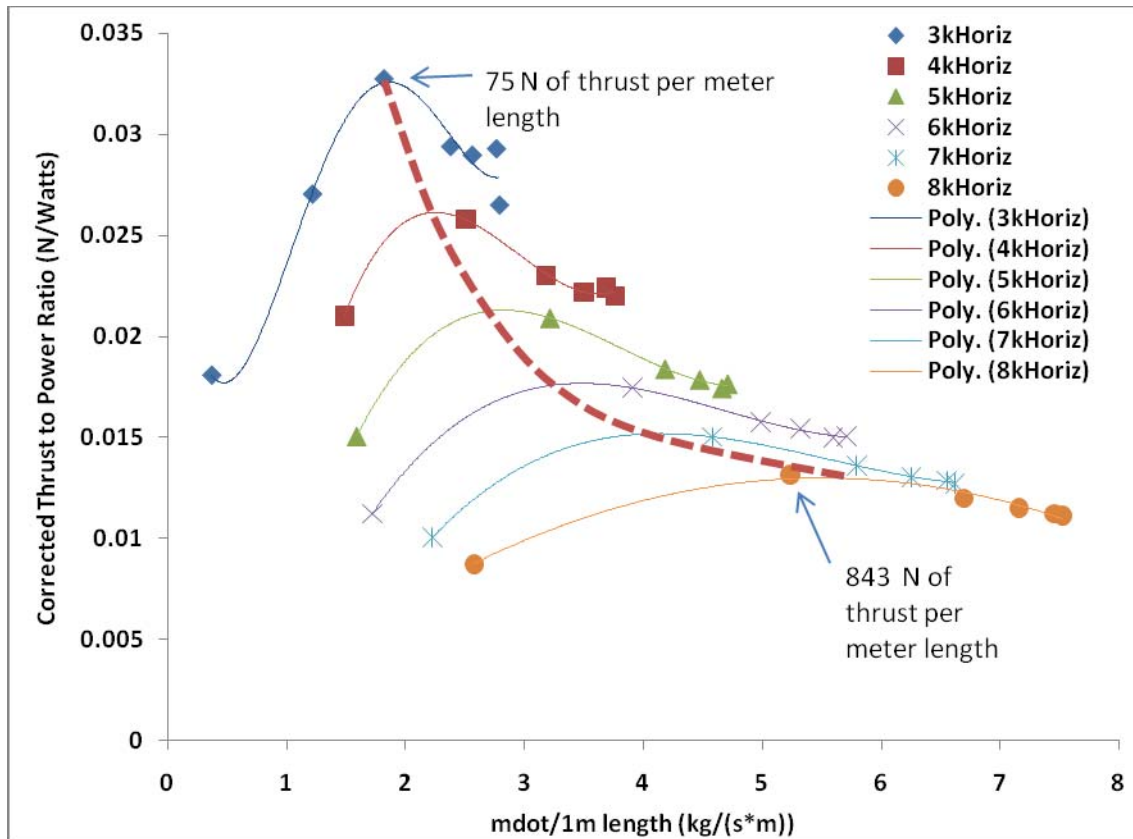
Figure 48.　　　Conceptual Operating Line using Data from the Horizontal Inlet
Experimental Configuration

APPENDIX A: MESH SETTINGS

This appendix details the specific settings applied using ANSYS CFX MESH applied to the baseline and subsequent models within ANSYS WORKBENCH. Details on mesh spacing, controls, and strategies can be found below.

A.   BASELINE CASING WITHOUT INFLATION

- Regions – The following regions were created/identified:

    o "ViscousWalls" – 14 2D Regions

    o "CasingInterface" – 1 2D Region

    o "Inlet" – 1 2D Region

    o "Outlet" – 1 2D Region

    o CasingSym1 – 1 2D Region

    o "CasingSym2" – 1 2D Region

- Mesh

    o Default Mesh Scale [in] – 0.89

    o Default Mesh Scale Factor [in] - 1

- Mesh Spacing

    o Default Body spacing – 0.89 inches maximum

    o Default Face spacing

        - Angular Resolution Option

        - Angular Resolution – 20 degrees

        - Minimum Edge Length [in] – 0.005

        - Maximum Edge Length [in] – 0.1

        - Radius of Influence [in] – 0

- Expansion Factor – 1.2

- Controls (Locations pictured in Figure 7 with typical refinement results shown in Figure 6)

  o Point Spacing 1

    ▪ Length Scale [in] – 0.01

    ▪ Radius of Influence [in] 0.125

    ▪ Expansion Factor – 1.2

  o Line Control 1,2,3,4 (as pictured in Figure XX)

    ▪ Uniform Spacing

    ▪ Point Spacing 1

- Stretch – 1 in X, Y, and Z

- Proximity

  o Edge Proximity – Yes

  o Surface Proximity – Yes

  o Elements Across Gaps – 1

  o Maximum number of Passes – 5

- Options

  o Global Mesh Scaling – 1

  o Surface Meshing – Delaunay

  o Meshing Strategy – Advancing Front and Inflation 3D

  o Volume Meshing – Advancing Front
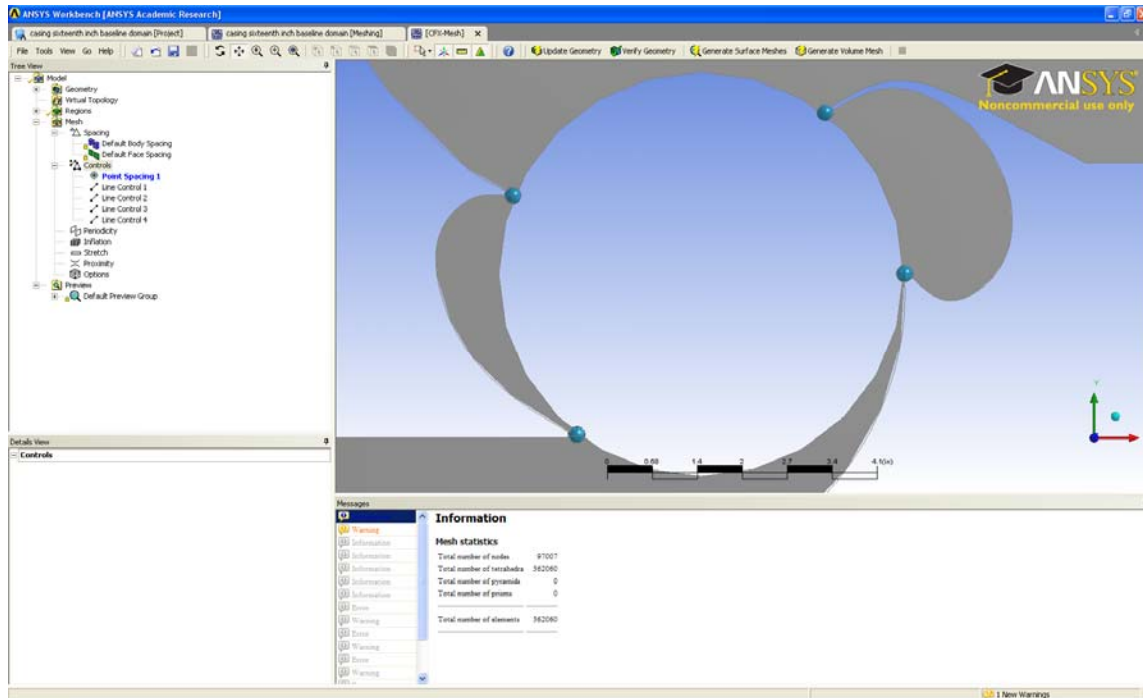
Figure 49.   Baseline Housing Showing Locations of Point Control Application

B.   BASELINE FAN WITHOUT INFLATION

- Regions – The following regions were created/identified:

    o "FanSym1 – 1 2D Region

    o "FanSym2" – 1 2D Region

    o "FanInterface" – 1 2D Region

    o "Blades" – 120 2D Regions

- Mesh

    o Default Mesh Scale [in] – 0.3

    o Default Mesh Scale Factor [in] - 1

- Mesh Spacing

    o Default Body spacing – 0.3 inches maximum

75

- o Default Face spacing

  - ▪ Angular Resolution Option

  - ▪ Angular Resolution – 20 degrees

  - ▪ Minimum Edge Length [in] – 0.001

  - ▪ Maximum Edge Length [in] – 0.3

  - ▪ Radius of Influence [in] – 0

  - ▪ Expansion Factor – 1.2

- Stretch – 1 in X, Y, and Z

- Proximity

  - o Edge Proximity – Yes

  - o Surface Proximity – Yes

  - o Elements Across Gaps – 1

  - o Maximum number of Passes – 5

- Options

  - o Global Mesh Scaling – 1

  - o Surface Meshing – Delaunay

  - o Meshing Strategy – Advancing Front and Inflation 3D

  - o Volume Meshing – Advancing Front

C. CASING WITH INFLATION

The addition of inflation layers on the baseline housing mesh at the viscous wall surfaces retained all of the previous mesh settings outlined previously except for the following:

- Inflation

    o Number of Inflated Layers – 5

    o Expansion Factor – 1.2

    o Number of Spreading Iterations – 0

    o Minimum Internal Angle [Degrees] – 2.5

    o Minimum External Angle [Degrees] – 10.0

    o Option – Total Thickness

    o Thickness Multiplier – 1

    o Maximum Thickness [in] – 0.005

D.   FAN WITH INFLATION

Similar to the casing, the fan region mesh was changed only in term of the inflation parameters:

- Inflation

    o Number of Inflated Layers – 7

    o Expansion Factor – 1.2

    o Number of Spreading Iterations – 0

    o Minimum Internal Angle [Degrees] – 2.5

    o Minimum External Angle [Degrees] – 10.0

    o Option – Total Thickness

    o Thickness Multiplier – 1

    o Maximum Thickness [in] – 0.01

E.   OTHER CASING VARIATIONS

The casings with horizontal inlets, missing cavities, and inlet guide vanes used the same meshing parameters as the baseline model with inflation layers added except for

one major difference. These casings used a 2D extruded meshing strategy instead of the earlier "Advancing Front and Inflation 3D" strategy. Additionally, the casing without cavities required different point controls, as illustrated in Figure 50, with Table 9 listing the vertices used to apply the point controls in the triangular regions.
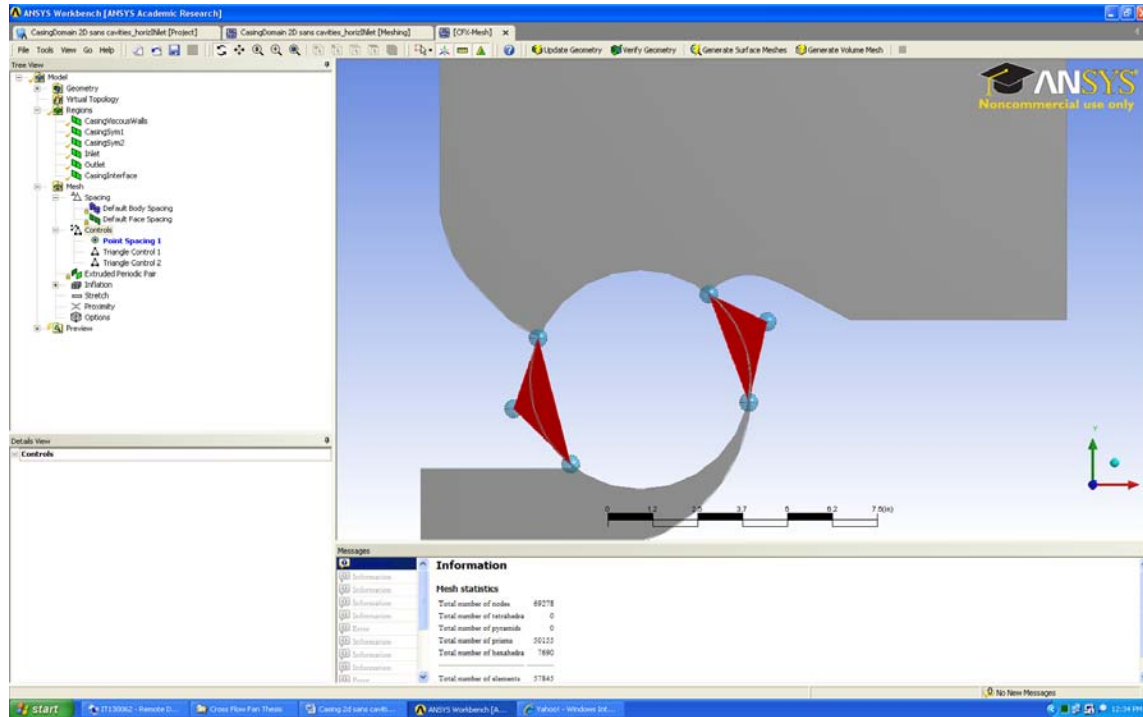
Figure 50.   Triangular area application of point controls for regional mesh refinement in ANSYS CFX MESH

Region	X	Y	Z
LPC	-1.92 [in]	-2.35 [in]	0.06 [in]
	-2.82 [in]	1.17 [in]	0.06 [in]
	-3.50 [in]	-0.81 [in]	0.06 [in]
HPC	1.89 [in]	2.37 [in]	0.06 [in]
	2.99 [in]	-0.64 [in]	0.06 [in]
	3.50 [in]	1.61 [in]	0.06 [in]

Table 9.   Triangle Point Control Vertex Locations for Model Without Cavities

78

APPENDIX B: ANSYS CFX PRE SETTINGS

Once the casing and fan meshes had been generated and imported into CFX-PRE, problem definition was accomplished. All models were run initially with default or solver chosen initial values through the first revolution. Additional revolutions for a total of ten were completed in one simulation to the extent practical (server issues limiting at times) with the results from the first revolution interpolated into the initial values file for the follow on simulation of revolutions two through ten. Details on the specific boundary conditions, solver settings, and equation classes used for the unmodified casing with inlet guide vanes is representative of all models ran and can be found below.

1ˢᵗ Revolution:

- Simulation Type - Basic Settings

    o External Solver Coupling - None

    o Simulation Type

        ▪ Option – Transient

    o Time Duration

        ▪ Option – Total Time

        ▪ Total Time – 0.02 [s] (depends on rotational speed and desired number of revolutions, e.g. 3000 rpm for 0.02 seconds yields 1 complete revolution)

    o Time Steps

        ▪ Option – Adaptive (used to control RMS Courant number. Despite ANSYS CFX being an implicit solver, transient solutions can be quite sensitive to Courant or CFL number)

        ▪ First Update Time – 0 [s]

        ▪ Timestep Update Freq –1

- Initial Timestep – 8e-006 [s]
  - o Timestep Adaptation
    - Option – RMS Courant Number
    - Minimum Timestep – 1e-006 [s]
    - Maximum Timestep – 0.001 [s]
    - Courant Number – 1
  - o Initial Time
    - Option – Automatic with Value
    - Time – 0 [s]
- Casing Domain – General Options
  - o Basic Settings
    - Location – Select the appropriate domain/mesh file for your casing domain region which depends on how you set it up in CFX Mesh
    - Domain Type – Fluid Domain
    - Fluids List – Air Ideal Gas
    - Coord Frame – Coord 0
  - o Domain Models
    - Pressure
      - Reference Pressure – 1 [atm]
    - Buoyancy
      - Option – Non Buoyant
    - Domain Motion
      - Option – Stationary

- Mesh Deformation

  - Option – None

- Casing Domain – Fluid Models

  o Heat Transfer

    - Option – Total Engergy

    - Incl. Viscous Work Term – checked

  o Turbulence

    - Option – k-Epsilon

    - Wall Function – Scalable

- Casing Domain – Initialization

  o Domain Initialization – unchecked

- Casing Domain Boundary Conditions (The names of the boundaries will vary depending on how you named the regions in CFX MESH)

  o CasingSym1

    - Boundary Type – Symmetry

    - Location – CasingSym1 (names available in the drop down list again depend on how you name the regions in CFX MESH)

  o CasingSym2

    - Boundary Type – Symmetry

    - Location – CasingSym2 (names available in the drop down list again depend on how you name the regions in CFX MESH)

  o CasingViscousWalls

    - Boundary Type – Wall

- Location – ViscousWalls ((names available in the drop down list again depend on how you name the regions in CFX MESH)

- Coord Frame – Unchecked

- Thin Surfaces

    - Create Thin Surface Partner – Unchecked

o Domain Interface 1 Side 1 – Basic Settings

- Boundary Type – Interface

- Location – (names available in the drop down list again depend on how you name the regions in CFX MESH)

- Coord Frame – Unchecked

o Domain Interface 1 Side 1 – Boundary Details (This boundary is added once a Domain Interface is added by right clicking on "Simulation" in the outline view in CFX PRE, selecting "Insert", and then selecting "Domain Interface")

- Mass and Momentum

    - Option – conservative Interface Flux

- Turbulence

    - Option – Conservative Interface Flux

- Heat Transfer

    - Option – Conservative Interface Flux

- Nonoverlap Conditions – Unchecked

o Inlet – Basic Settings

- Boundary Type – Opening

- Location – Inlet (names available in the drop down list again depend on how you name the regions in CFX MESH)

- Coord Frame – Unchecked

o Inlet – Boundary Details

- Flow Regime

  - Option – Subsonic

- Mass And Momentum

  - Option – Opening Pres. And Dirn

  - Relative Pressure – 0 [Pa]

- Flow Direction

  - Option – Normal to Boundary Condition

- Loss Coefficient – Unchecked

- Turbulence

  - Option – Medium (Intensity = 5%)

- Heat Transfer

  - Option – Static Temperature

  - Static Temperature – 300 [K]

o Outlet – Basic Settings

- Boundary Type – Opening

- Location – Outlet (names available in the drop down list again depend on how you name the regions in CFX MESH)

- Coord Frame – Unchecked

o Outlet – Boundary Details

- Flow Regime

- Option – Subsonic

- Mass and Momentum

  - Option – Opening Pres. and Dirn

  - Relative Pressure – 0 [Pa]

- Flow Direction

  - Option – Normal to Boundary Condition

- Loss Coefficient – Unchecked

- Turbulence

  - Option – Medium (Intensity = 5%)

- Heat Transfer

  - Option – Static Temperature

  - Static Temperature – 300 [K]

o ViscousIGVWalls – Basic Setting

- Boundary Type – Wall

- Location – ViscousIGVWalls (names available in the drop down list again depend on how you name the regions in CFX MESH)

- Coord Frame – Unchecked

o ViscousIGVWalls – Boundary Details

- Wall Influence on Flow

  - Option – No Slip

  - Wall Velocity – Unchecked

- Wall Roughness

  - Option – Smooth Wall

84

- Heat Transfer

  - Option – Adiabatic

- Fan Domain – General Options

  o Basic Settings

    - Location -- (names available in the drop down list again depend on how you name the regions in CFX MESH)

    - Domain Type – Fluid Domain

    - Fluids List – Air Ideal Gas

    - Coord Frame – Coord 0

    - Particle Tracking – Unchecked

  o Domain Models

    - Pressure

      - Reference Pressure – 1 [atm]

    - Buoyancy

      - Option – Non Buoyant

    - Domain Motion

      - Option – Rotating

      - Angular Velocity – (-)3000 [rev min^-1] (+/- depends on how you set your global axis reference when building the solid model)

      - Alternate Rotation Model – Unchecked

      - Axis Definition

        o Option – Coordinate Axis

        o Rotation Axis – Global Z

- Mesh Deformation

    o Option – None

- Fan Domain – Fluid Models

    o Heat Transfer

        ▪ Option – total energy

        ▪ Incl. Viscous Work Term – Checked

    o Turbulence

        ▪ Option – k-Epsilon

        ▪ Wall Function – Scalable

- Fan Domain – Initialization

    o Domain Initialization – unchecked

- Fan Domain – Boundary Conditions (The names of the boundaries will vary depending on how you named the regions in CFX MESH)

    o Blades – Basic Settings

        ▪ Boundary Type – Wall

        ▪ Location – Blades (names available in the drop down list again depend on how you name the regions in CFX MESH)

        ▪ Coord Frame – Unchecked

        ▪ Frame Type – Rotating

    o Blades – Boundary Details

        ▪ Wall Influence On Flow

            • Option – No Slip

            • Wall Velocity – Unchecked

        ▪ Wall Roughness

- Option – Smooth Wall
    - ▪ Heat Transfer
        - Option – Adiabatic
- o Domain Interface 1 Side 2 – Basic Settings
    - ▪ Boundary Type – Interface
    - ▪ Location – (names available in the drop down list again depend on how you name the regions in CFX MESH)
    - ▪ Coord Frame – Unchecked
- o Domain Interface 1 Side 2 – Boundary Details
    - ▪ Mass and Momentum
        - Option – conservative Interface Flux
    - ▪ Turbulence
        - Option – Conservative Interface Flux
    - ▪ Heat Transfer
        - Option – Conservative Interface Flux
        - Nonoverlap Conditions – Unchecked
- o FanSym1
    - ▪ Boundary Type – Symmetry
    - ▪ Location – FanSym1 (names available in the drop down list again depend on how you name the regions in CFX MESH)
- o FanSym2
    - ▪ Boundary Type – Symmetry
    - ▪ Location – FanSym2 (names available in the drop down list again depend on how you name the regions in CFX MESH)

- Domain Interface 1

    o Interface Type – Fluid Fluid

    o Interface Side 1

        ▪ Domain (Filter) – CasingDomain (names available in the drop down list again depend on how you name the regions in CFX MESH)

        ▪ Region List – CasingInterface (names available in the drop down list again depend on how you name the regions in CFX MESH)

    o Interface Side 2

        ▪ Domain (Filter) – FanDomain (names available in the drop down list again depend on how you name the regions in CFX MESH)

        ▪ Region List – FanInterface (names available in the drop down list again depend on how you name the regions in CFX MESH)

    o Interface Models

        ▪ Option – General Connection

        ▪ Frame Change/Mixing Model

            • Option – Transient Rotor Stator

        ▪ Pitch Change

            • Option – Automatic

        ▪ Mass and Momentum – Unchecked

    o Mesh Connection Method

        ▪ Option – GGI

88

- Solver Control – Basic Settings

  o Advection Scheme

    ▪ Option – Upwind

  o Transient Scheme

    ▪ Option – Second Order Backward Euler

    ▪ Timestep Initialization

      • Option – Automatic

      • Lower Courant Number – Unchecked

      • Upper Courant Number – Unchecked

  o Convergence Control

    ▪ Minimum Number of Coefficient Loops – Unchecked

    ▪ Max. Coeff. Loops – 3

    ▪ Fluid Timescale

      • Timescale control – Coefficient Loops

  o Convergence Criteria

    ▪ Residual Type – RMS

    ▪ Residual Target – 1.E-4

    ▪ Conservation Target – Unchecked

  o Elapsed Time Control – Unchecked

- Solver Control -- Advanced Options

  o Compressibility Control – Checked

    ▪ Total Pressure Option – Unchecked

  o High Speed Numerics – Checked

- Output Control

- o Trn Results Tab

  - ▪ Transient Results

    - • Select "add new item" button if nothing is indicated and accept default name of "Transient Results 1"

    - • Transient Results 1

      - o Option – Standard

      - o File Compression – Default

      - o Output Boundary Flows – Unchecked

      - o Output Equation Residuals – Unchecked

      - o Output Frequency

        - ▪ Option – Time Interval

        - ▪ Time Interval – 0.005 [s] (chosen by user; in this case due to the large file size and lengthy processor down time for writing the file, I chose to have a transient results file written every 90 degrees of rotation which translates to every 0.005 seconds when rotating at 3,000 rpm)

- • Expert Parameters (In order to insert an Expert Parameter, user must first select "Insert" from main menu, then select "Solver," then Select "Expert Parameter")

  - o I/O Control Tab

    - ▪ Transient Model and I/o

    - ▪ Transient initialization override – Checked

    - ▪ Transient initialization o – t

- Select "Write Solver File" Icon in top menu

  o Save the *.def file in your chosen location

  o Solver Menu

    - Select mode of processing

      - PVM Local Parallel

      - PVM Distributed Parallel

      - Etc.

    - Select number of mesh partitions

    - Select Location to write results file

    - Click "Start Run"

Follow on Revolutions or Resuming a Simulation

- Select the appropriate *.pre file

- Adjust time duration as necessary

- Select "Write Solver File" Icon in top menu

  o Save the *.def file in your chosen location

  o Solver Menu

    - Initial Values File – select appropriate *.res or *.trn file from which you are resuming the simulation from.

    - Interpolate Initial Values onto Def File Mesh – Checked

    - Select mode of processing

      - PVM Local Parallel

      - PVM Distributed Parallel

      - Etc.

    - Select number of mesh partitions

- Select Location to write results file

- Click "Start Run"

APPENDIX C

The 7 IGV model with a modified inlet, fan inlet arc of 130 degrees vice 105 degrees and no cavities was developed in an effort to address areas of concern that were observed after the 6IGV model was analyzed with ANSYS CFX. Referring back to Figure 28 in Chapter IV.A.1, it was observed that the IGVs located towards the left hand side of the housing appeared to be developing lift. In an effort to address this, the inlet housing was contoured to aid in shaping the flow field while the fan inlet arc was increased and one additional IGV was added for a total of seven.

The 6 IGV model also displayed relatively poor efficiency performance. To address this, it was thought that removal of the cavities should improve efficiency as has been observed by Cheng [4] and Kummer [10]. The removal of the cavities also allowed for widening the inlet arc, which was thought may alleviate the decreased mass flow rate usually observed when eliminating the cavities.

Referring back to Table 7 presented in Chapter IV.A, the 7 IGV model with its modified inlet and housing only improved over the 6 IGV model in terms of total temperature ratio. Efficiency, mass flow rate, total pressure, and thrust per unit length of span were all down from the 6 IGV model.

Since there was more than one design attribute changed from any previous model when there 7 IGV model was created, analysis as to what design attribute led to the poor performance is difficult at best. Further implicating that the IGV design and implementation is a major contributor to poor performance, Figure 51 shows the velocity vectors near the IGVs. It appears as though in comparison to Figure 28, the problem of IGV induced lift has now shifted from the far left to the far right. Further, it would appear that elimination of the IGV furthest to the right may provide some improvement. However, given the results of IGV application, that effort may not be worthwhile.
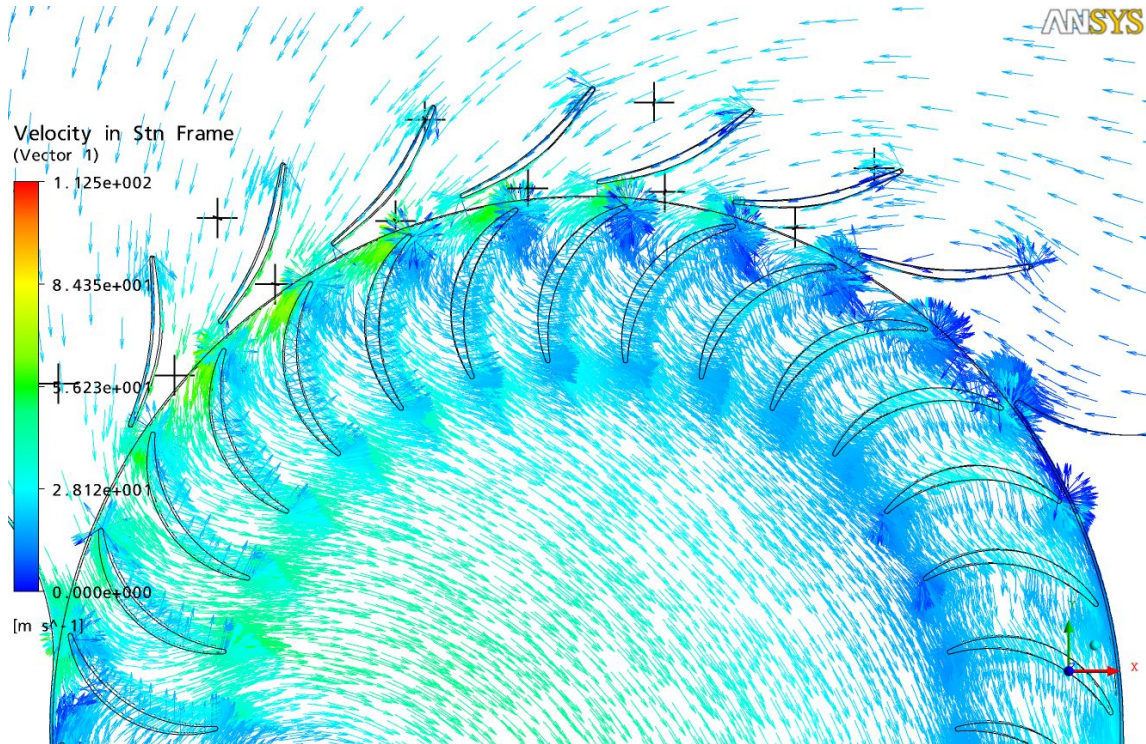
Figure 51.   Velocity Vectors near the IGVs for the 7 IGV CFD Model

LIST OF REFERENCES

[1]   P. Mortier, "Fan or Blowing Apparatus," U.S. Patent No. 507,445, filed 1893.

[2]   Naval Air Systems Command contract N00019-74-C-0434, *Multi-Bypass Ratio System Technology Development,* Vol. I-III, Vought Systems Division, LTV Aerospace Corporation, 24 July 1975.

[3]   M. Seaton, "Performance Measurements, Flow Visualization, and Numerical Simulation of a Crossflow Fan," Master's thesis, Department of Aeronautics and Astronautics, Naval Postgraduate School, March 2003.

[4]   W. Cheng, "Experimental and Numerical Analysis of a Crossflow fan," Master's thesis, Department of Aeronautics and Astronautics, Naval Postgraduate School, December 2003.

[5]   C. Schreiber, "Effect of Span Variation on the Performance of a Cross Flow Fan," Master's thesis, Department of Aeronautics and Astronautics, Naval Postgraduate School, June 2006.

[6]   H. Yu, "Experimental Investigation and Numerical Prediction of a Crossflow Fan," Master's thesis, Department of Aeronautics and Astronautics, Naval Postgraduate School, December 2006.

[7]   J. Ulvin, "Experimental Investigation of a Six Inch Diameter, Four Inch Span Cross-Flow Fan," Master's thesis, Department of Aeronautics and Astronautics, Naval Postgraduate School, June 2008.

[8]   A. Gannon, J. M. Utschig, G. V. Hobson, and M. F. Platzer, "Experimental Investigation of a Small-Scale Cross-Flow Fan for Aircraft Propulsion," presented February 2006.

[9]   P. Peebles, "Aerodynamic Lift Generating Device," U.S. Patent No. 6,527,229 B1, March 2003. See also www.fanwing.com.

[10]   J. Kummer, "Simulation of the Cross Flow Fan and Application to a Propulsive Airfoil Concept," Doctoral Dissertation, Department of Mechanical and Aerospace Engineering, Syracuse University, August 2006.

[11]   J. Kummer, and T. Dang, "High Lift Propulsive Airfoil with Integrated Crossflow Fan," *Journal of Aircraft* Vol. 43, No. 4, July–August 2006.

[12]   D. Gossett, "Investigation of Cross Flow Fan Propulsion for Lightweight VTOL Aircraft," Master's Thesis, Department of Aeronautics and Astronautics, Naval Postgraduate School, Monterey, CA, December 2000.

[13]   Muson, Young, Okiishi, *Fundamentals of Fluid Mechanics*, Fifth Edition, Hoboken, NJ, 2006.

[14]   NACA Report 1135, Equations, Table and Charts for Compressible Flow, 1953.

THIS PAGE INTENTIONALLY LEFT BLANK

INITIAL DISTRIBUTION LIST

1.   Defense Technical Information Center
   Ft. Belvoir, Virginia

2.   Dudley Knox Library
   Naval Postgraduate School
   Monterey, California

3.   Prof. Garth V. Hobson
   Department of Mechanical and Astronautical Engineering
   Naval Postgraduate School
   Monterey, California

4.   Prof. Anthony J. Gannon
   Department of Mechanical and Astronautical Engineering
   Naval Postgraduate School
   Monterey, California

5.   Samuel F. Cordero
   Monterey, California